Catalysis Today 453 (2025) 115261

Contents lists available at ScienceDirect

Catalysis Today

journal homepage: www.elsevier.com/locate/cattod

Mg-modified Ni-based catalysts prepared by the solution combustion synthesis for dry reforming of methane

Alua M. Manabayeva [a,b,d,*], Päivi Mäki-Arvela [b], Zuzana Vajglová [b], Mark Martinéz-Klimov [b], Olha Yevdokimova [b], Anssi Peuronen [c], Mika Lastusaari [c], Teija Tirri [b], Svetlana A. Tungatarova [d,e], Tolkyn S. Baizhumanova [d,e], Kaisar Kassymkan [d], Gulnar N. Kaumenova [d], Manapkhan Zhumabek [d], Daulet A. Zhumadullaev [d], Dinmukhamed Shoganbek [d,e], Dmitry Yu. Murzin [b,d,**]

[a] Kazakh-British Technical University, Almaty, Kazakhstan
[b] Laboratory of Industrial Chemistry and Reaction Engineering, Åbo Akademi University, Turku, Finland
[c] University of Turku, Department of Chemistry, Turku FI-20014, Finland
[d] D.V. Sokolsky Institute of Fuel, Catalysis and Electrochemistry, Almaty, Kazakhstan
[e] Al-Farabi Kazakh National University, Almaty, Kazakhstan

ARTICLE INFO

Keywords:
Dry reforming
Methane
Solution combustion
Mg modified
Ni catalysts

ABSTRACT

In the current work, nickel and magnesia containing catalysts synthesized by solution combustion synthesis (SCS) and impregnation were used for dry reforming of methane (DRM). The present research showcased the difference of two preparation methods and demonstrated the influence of temperature cycling and various duration on the activity of Ni-Mg catalysts (30 min, 10 h, 20 h, 200 h TOS). It was reported that Ni-Mg-Al catalysts exhibited mainly crystalline $MgAl_2O_4$ and nickel oxide in both fresh and spent catalysts confirmed by XRD results. As seen from TEM images, nickel particles ranged from 12 to 36 nm. Small metal particles indicate the strong interactions between the metal and the support. Moreover, these particles were localized at the tip of carbon nanotube indicating their activity. According to TPD, for all catalysts large amounts of basic sites and strong interactions between the metal and CO_2 were observed. Ni-Mg-Al obtained with SCS possesses 0.19 wt%·g_{Ni}^{-1} of carbon content, which was much lower than that of Ni-Mg catalyst. It was found that SCS derived Ni-Mg-Al catalyst exhibited higher activity compared to its reduced analogue prepared by impregnation. The former catalyst showed stable performance during 200 h test with a decreasing coking rate. The metal particle size was lower for this spent catalyst in comparison with Ni-Mg-Al tested for 20 h test.

1. Introduction

The rising levels of carbon dioxide in atmosphere improve global warming. On the other hand, the exhaustion of fossil fuel resources has driven significant investigation into advanced methods for production of sustainable energy. Among other methane reforming processes, dry reforming of methane (DRM) has been considering as a viable approach to utilize CH_4 and CO_2 and to produce valuable syngas, which has various applications [1–3].

Eq. (1) demonstrates the main DRM reaction with production of synthesis gas in the ratio of H_2/CO of unity. This ratio allows application of the gaseous products to obtain dimethyl ether.

$$CH_4 + CO_2 \rightarrow 2CO + 2H_2;\ \Delta H_0^{298} = +248\ kJ{\cdot}mol^{-1} \quad (1)$$

The role of DRM for industry has been stuFdied since ecological problems could be solved when converting biogas (methane and carbon dioxide) to hydrogen and CO. However, for this process elevated temperatures are mandatory because of its endothermicity. Formation of coke could be a second issue in conducting DRM. Coke is accumulated during the side reaction such as methane cracking (Eq. (3)) and Boudouard reaction (Eq. (2)) [4]. Coke deposition from methane cracking is more possible than from the latter reaction. Reverse water-gas shift

* Corresponding author at: Kazakh-British Technical University, Almaty, Kazakhstan.
** Corresponding author at: Laboratory of Industrial Chemistry and Reaction Engineering, Åbo Akademi University, Turku, Finland.
E-mail addresses: manabaeva_2018@mail.ru (A.M. Manabayeva), dmitry.murzin@abo.fi (D.Yu. Murzin).

https://doi.org/10.1016/j.cattod.2025.115261
Received 22 October 2024; Received in revised form 24 February 2025; Accepted 2 March 2025
Available online 4 March 2025

reaction (RWGS) occurs during DRM consuming more hydrogen and CO_2 and presented in Eq. (4) [5].

$$2CO \rightleftharpoons CO_2 + C;\ \Delta H_0^{298} = -172\ kJ{\cdot}mol^{-1} \quad (2)$$

$$CH_4 \rightarrow C + 2H_2;\ \Delta H_0^{298} = +75\ kJ{\cdot}mol^{-1} \quad (3)$$

$$CO_2 + H_2 \rightleftharpoons CO + H_2O;\ \Delta H_0^{298} = +42\ kJ{\cdot}mol^{-1} \quad (4)$$

In past decades, effective catalysts were developed since efficiency and stability of DRM process are strongly affected by the catalytic system. Although nickel-based catalysts are cost-effective and catalytically active, they often undergo deactivation like sintering and coke deposition [6]. To enhance the activity and longevity of Ni catalysts, various modifications have been explored, including the incorporation of alkali earth metals. They are considered as good promoters in improving catalytic activity of Ni/Al_2O_3 because they can enhance reducibility and strong metal-support interactions. Mg, Ca, Sr provides basicity to the nickel catalysts leading to their resistance to coke formation [7]. Magnesium has shown a promise in improving catalyst stability during DRM [8]. For example, Ni55Mg11Al exhibited initial CH_4 conversion of 94 %, which is 24 % higher than that of NiAl without a promoter [9,10].

Modification of the Ni-based catalysts with Mg in the present work enhancing interactions between NiO and $MgAl_2O_4$ hindered nickel particles from moving away from the support and their encapsulation by coke [11]. Due to its basicity, Ni-Mg-Al catalysts can be catalytically stable during long-periods under the reactant flow [12]. In comparison with γ-Al_2O_3 $MgAl_2O_4$ exhibits better resistance to sintering and thus to coking.

Table 1 shows comparative results from different studies. In [13] stable NiO/MgO–ZrO_2 catalyst demonstrated conversion of ca. 85 % throughout 60 h, because metal-support interactions were strong and Ni particles were well dispersed. Similar activity was observed also for Ni-5Mg-MSC at 850 °C within 14 h [14]. The surface area determined by BET method was different for all catalysts indicating that it does not have an influence on catalytic activity. Presence of Al enhances the reducibility of Ni in the MgNiAl-2.0 catalyst exhibiting a higher conversion for longer duration [15]. Promotion of NiMgAl with Zn in small amounts declined carbon deposition to 5 %, enhanced catalytic activity due to a high metal dispersion, while addition of Zn in larger amounts caused blocking of Ni active sites [16].

Magnesium aluminate spinel is usually used in DRM as a thermostable support. Furthermore, it improves resistance to carbon formation exhibiting high basicity [17]. In [18] $MgAl_2O_4$ was synthesized by the co-precipitation method at a high temperature, taking a long-time. Alternatively, as a fast and effective preparation method, solution combustion synthesis can be applied, when $MgAl_2O_4$ phase can be formed at lower temperatures. For instance, at a pre-ignition temperature of 500 °C metal nitrates can be burnt by such fuels as glycine or urea [19].

Currently, the solution combustion synthesis is considered as promising method being already applied for various reactions like CO_2 methanation [20–22], partial oxidation of methane [23], dry reforming of methane [24], steam reforming of methane [25], CO_2 reduction to CO [26]. This method has several advantages, i.e. a rapid preparation of the materials, and a high heat release at a short combustion time. The preparation of catalysts includes dissolution of the oxidizing agents (metal nitrates) and fuel in water. The nitrates are used because they are highly soluble and have low melting points. The fuels are typically nitrogen-containing organic compounds (urea, glycine, citric acid, etc.) initiating combustion and causing flame. In some cases, the flame is not observed [25]. The flame temperature is higher than the initial temperature. Finally, at the end of the synthesis procedure, the oxide materials are obtained.

This study aims to delve into the DRM over Ni-Mg-Al catalysts synthesized by the solution combustion and wet impregnation methods. Characterization techniques (XRD, SEM, TEM, nitrogen physisorption, TPR and TPD) and catalytic performance of these catalysts were explored. Coking was evaluated by TGA, CHNS, and TPO analyses.

2. Experimental

2.1. Catalyst synthesis

For the solution combustion synthesis, highly soluble metal nitrates were used. Urea ($CO(NH_2)_2$) was applied as the fuel for combustion. The oxidizer/fuel ratio was taken as unity according to [27]. 3 g of Ni $(NO_3)_2{\cdot}6\ H_2O$ (97 %, Sigma Aldrich), 3 g of $Mg(NO_3)_2{\cdot}6\ H_2O$ (99 %, Sigma Aldrich), 4 g of $Al(NO_3)_3{\cdot}9\ H_2O$ (99 %, Carlo Erba) and 10 g of urea (99.5 %, Sigma Aldrich) were dissolved in ca. 30 mL deionized water pre-heated at 80 °C, thereafter thoroughly mixed to achieve homogeneity. The obtained solution was transferred to a muffle furnace, set at 500 °C required for the combustion process. Combustion proceeded for 10–15 min, during which the exothermic reaction occurred, resulting in generation of the desired 15Ni-15Mg-20Al catalyst. 15Ni-35Mg sample was prepared in a similar manner.

Incipient wetness impregnation was used as a comparable method. γ-Al_2O_3 was dried beforehand at 250 °C for 1 h to remove moisture. An aqueous solution of 2.4 mL of $Ni(NO_3)_2{\cdot}6\ H_2O$ (97 %, Sigma Aldrich) and 1.1 mL of $Mg(NO_3)_2{\cdot}6\ H_2O$ (99 %, Sigma Aldrich) was impregnated onto the dried 4.11 g of γ-Al_2O_3. Masses of pure Ni and Mg were 0.61 g and 0.28 g, respectively. After impregnation, the sample underwent drying at 250 °C for 1.5 h to remove the excess of the solvent. Thereafter, the impregnated material was calcined at 650 °C for 3 h to obtain the final 12 wt% Ni-6 wt% Mg/γ-Al_2O_3 catalyst.

Prior to the DRM test, calcined 12 wt% Ni-6 wt% Mg/γ-Al_2O_3 catalyst was activated in hydrogen atmosphere under 40 mL·min^{-1} for 20 min at 900 °C and flushed with an inert gas (Ar) from hydrogen traces at 70 mL·min^{-1} for 40 min, then cooled down to the room temperature.

2.2. Catalyst characterization

The crystal structure and phase composition of the prepared and used catalysts were analyzed using X-ray diffraction (XRD) on a DRON-4.07 diffractometer. The instrument was equipped with a cobalt X-ray

Table 1
Comparative results of different catalysts used in DRM.

Entry	Catalyst	Reaction conditions	X_{CH4}, %	X_{CO2}, %	H_2/CO	S_{BET} $m^2{\cdot}g^{-1}$	Metal particle size, nm	TOS, h	Ref.
1	10 wt% NiO/MgO–ZrO_2	CH_4:CO_2= 1:1, 700 °C, GHSV= 267 mL $min^{-1}g^{-1}$	85	86	1.0	29.9	n.a.	60	[13]
2	Ni−5Mg-MSC	CH_4:CO_2= 1:1, 850 °C, GHSV= 300 mL min^{-1} g^{-1}	84.7	86.5	1.0	553	n.a.	14	[14]
3	MgNiAl−2.0	N_2:CH_4:CO_2= 20:10:20, 850 °C, GHSV= 667 mL min^{-1} g^{-1}	90	98	1.4	100	13.11	200	[15]
4	NiMgAl−3Zn	CH_4:CO_2= 1:1, 650 °C, flow rate = 3000 mL min^{-1} g^{-1}, 10 mg catalyst	[a]0.107	[a]0.116	0.9	153	9.5	100	[16]

Note:
[a] - mol·$min^{-1}{\cdot}g_{cat}^{-1}$

tube, giving irradiation with a characteristic wavelength of 1.78892 Å. The analysis was carried out over a range of diffraction angles, from 5° to 100°. HighScore Plus software and the PDF-4 + database were used to facilitate the phase identification [28,29].

The morphology and surface characteristics of the catalysts were examined using a Zeiss Leo Gemini 1530 Scanning Electron Microscope (SEM), supplied with a Thermo Scientific UltraDry Silicon Drift Detector (SDD) for energy-dispersive X-ray spectroscopy (EDS) analysis. The acceleration voltage of 30 kV was used for elemental analysis.

The textural properties of the catalysts were characterized by liquid nitrogen physisorption using a Micromeritics 3Flex-3500 instrument. The measurements were performed at liquid nitrogen temperature (-196°C) to analyze the surface area, pore volume, and pore size distribution of the samples. The moisture was removed from ca. 0.15 g catalysts by drying. After degassing for 20 h at 180 ºC, the samples were pre-treated under vacuum for 5 h at 180°C to ensure complete removal of adsorbates from the surface. During this stage the relative pressures varied and liquid nitrogen was adsorbed at −196 °C. The surface area was defined by the BET method, while the pore size distribution was calculated with NLDFT method.

The size and morphology of the Ni particles in the catalysts were characterized using a Jeol JEM-1400Plus Transmission Electron Microscope (TEM) equipped with an OsisQuemesa 11 Mpix bottom-mounted digital camera for 120 kV accelerating voltage and 0.38 nm resolution imaging. The catalysts were reduced beforehand by passing 30–40 mL·min^{-1} of hydrogen over the sample at 450 °C for 2 h. The heating rate during reduction was controlled at 10°C·min^{-1}. The TEM micrographs obtained were analyzed using ImageJ software to measure the Ni particle size distribution.

MicrotracBelcat II apparatus was used for TPR, TPD and TPO measurements.

Temperature-programmed reduction (TPR) was used to analyze the reducibility of the catalysts with a quartz tube reactor supplied with a thermal conductivity detector (TCD) to monitor hydrogen consumption during reduction. Ca. 100 mg sample was first pre-treated at 200 °C for 2 h under an inert argon atmosphere to remove any adsorbed gases or moisture. A gas mixture containing 5 vol% H_2 and 95 vol% Ar was introduced into the reactor. The flow rate was controlled at 1.5 mL·min^{-1} H_2 and 28.5 mL·min^{-1} Ar. The temperature was then gradually increased from 50°C to 800 °C at a rate of 10 °C·min^{-1}. The targeted temperature was held constant for 20 min.

The acidity of the catalyst was examined using ammonia temperature programmed desorption (NH_3-TPD) to assess the strength and quantity of the acid sites. Ca. 60–100 mg of the catalyst underwent heating to 500 °C for 1 h to remove any pre-adsorbed species from the surface and cooled to 50 °C. Then, the sample was exposed to NH_3 at 100 °C for 30 min. After NH_3 adsorption, the sample was purged with He for 1 h. The temperature was gradually increased from 50 °C to 600 °C at a heating rate of 10 °C·min^{-1} while maintaining a flow of 1.5 mL·min^{-1} NH_3 (5 vol%) and 28.5 mL·min^{-1} He (95 vol%). The temperature was held at 600 °C for 20 min.

Basicity of the catalyst was studied using CO_2 temperature programmed desorption (CO_2-TPD) to evaluate the nature and strength of basic sites. The catalyst was dried by heating it to 150 °C for 30 min under a helium flow to remove adsorbed moisture or gases from the surface. After cooling to 50 °C adsorption of CO_2 took place on the sample surface for 30 min. Then, the sample was flushed at 50 °C for another 30 min, followed by heating from 50 °C to 700 °C at a ramp rate of 10°C·min^{-1} under a helium flow.

Oxidation of the catalysts was performed using O_2-temperature programmed oxidation (O_2-TPO). Pretreatment was conducted on ca. 50 mg of the spent catalyst at 300 °C for 2 h. After cooling to 50 °C, the temperature elevated to 865 °C with a ramp rate of 10 °C·min^{-1} under streams of gas mixture containing 1.5 mL/min and 28.5 mL·min^{-1} of oxygen (5 vol%) and Ar (95 vol%), respectively. At the target temperature the holding time was 20 min. By analyzing the concentrations of CO and CO_2 over time, the total amount of coke present on the catalyst can be estimated using a mass spectrometer (OmniStar, Pfeiffer), which was linked to the MicrotracBelcat II apparatus.

The analysis of carbon, hydrogen, nitrogen, and sulfur (CHNS) in the spent catalysts was performed using a Thermo Fisher Scientific Flash 2000 Organic Elemental Analyzer, which operates at 950 °C. Two columns are used for the separation and detection of different elements after oxidation and reduction processes. Moisture was removed from catalyst surface. The following standards were used for tests: cystine, 2,5-bis(5-tert-butyl-benzoxazol-2-yl)thiophene, sulphanilimide and methionine.

Thermogravimetric (TGA) and differential thermal analysis (DTA) of the spent catalysts was carried out using an SDT Q600 apparatus (TA Instruments) to measure the coke amount and type under N_2 or air atmosphere with flow of 100 mL·min^{-1} and the heating rate of 10 °C·min^{-1} close to the optimal DRM temperature of 800 °C.

2.3. Catalytic experiments

Evaluation of the catalytic performance in DRM was conducted in the fixed bed quartz tube reactor with the following parameters: 5 mm ID and 20 mm length. The catalyst, ca. 2 mL in volume, was placed within the reactor between layers of glass wool and quartz sand (2 mL at the bottom and 2 mL above the catalyst). The reacting gas stream (CH_4:CO_2:Ar = 1:1:1) was introduced to the catalyst at the required space velocity of 3000 h^{-1} (total flow rate of 100 mL·min^{-1}). The reaction temperature ranged in 600–900 °C with an increment of 50°C returning finally to 600 °C. At each target temperature, the catalyst was held for 15 min, and the reaction products were analyzed. Stability examination was carried out at 850 °C.

2.4. Analysis

For analysis of the initial gas mixture and the products, a Chromos GC-1000 chromatograph equipped with the Chromos software and two different columns was used. The packed column paired with a thermal conductivity detector was applied to detect gases such as hydrogen, oxygen, and nitrogen and was filled with Activated Carbon-3, with argon as the carrier gas at a flow rate of 10 mL·min^{-1}. The column had a length of 2 m and a diameter of 3 mm, and operated at 40 °C. The capillary column with a flame ionization detector was packed with XSEP sorbent, and air was used as the carrier gas at a flow rate of 200 mL·min^{-1}. This column, with a length of 3 m and a diameter of 3 mm, was operated at 200 °C and was used to identify carbon-based components, such as methane and carbon oxides.

2.5. Definitions

Conversion (X) and transformation rates of CH_4 and CO_2 (r), the space-time yield (STY) of H_2 and CO as well as their ratio were defined as follows (Eqs. (5–11)):

$$X_{CH4} = \frac{(F_{CH4,in} - F_{CH4,out})}{F_{CH4,in}} \times 100\% \quad (5)$$

$$X_{CO2} = \frac{(F_{CO2,in} - F_{CO2,out})}{F_{CO2,in}} \times 100\% \quad (6)$$

$$r_{CH4} = \frac{F_{CH4,in} - F_{CH4,out}}{m_{Co}} \quad (7)$$

$$r_{CO2} = \frac{F_{CO2,in} - F_{CHO2,out}}{m_{Co}} \quad (8)$$

$$STY_{H2} = \frac{F_{H2,out}}{m_{Ni}} \quad (9)$$

$$STY_{CO} = \frac{F_{CO,out}}{m_{Ni}} \quad (10)$$

$$H_2 \Big/ CO = \frac{STY_{H2}}{STY_{CO}} \quad (11)$$

where F_i is a molar flow of component *i*.

The carbon balance was calculated taking into account the molar flows of carbon-based components (Eq. (12)) [30]:

$$carbon\ balance = \frac{F_{CH4,out} + F_{CO2,out} + F_{CO,out}}{F_{CH4,in} + F_{CO2,\ in}} \quad (12)$$

The binary diffusivity (D_{AB})) determined using the Chapman-Enskog equation [31] was equal to $1.69{\cdot}10^{-4}$ $m^2{\cdot}s^{-1}$ for CH_4 and CO_2 respectively. The pore radius of 10 nm for 15Ni-15Mg-20Al catalyst (from BJH method using nitrogen physisorption) was taken into consideration calculating the Knudsen diffusivity (D_K= $6.90{\cdot}10^{-6}$ $m^2{\cdot}s^{-1}$ for CH_4). Thereafter, effective diffusion coefficient (D_e) was determined as $0.42{\cdot}10^{-6}$ $m^2{\cdot}s^{-1}$ from the Bosanquet equation. Considering that the ratio of porosity to tortuosity $\frac{\varepsilon}{\tau}$ is 0. 1, the effective diffusivity (D_{eff}) was defined using Eq. (13):

$$D_{eff} = \frac{\varepsilon}{\tau} D_e \quad (13)$$

As a result, D_{eff} was calculated to be $4.19{\cdot}10^{-7}$ $m^2{\cdot}s^{-1}$.

The Weisz-Prater parameter ϕ was calculated from:

$$\varphi = \frac{r_{obs} r_P^2 RT}{p_{CH4} D_{eff}} \leq 1 \quad (14)$$

where, r_p^2 is the radius of the catalyst particle, r_{obs} is the observed reaction rate, p is the CH_4 partial pressure, D_{eff} is the effective diffusivity.

It is important to stress that that the tests in the current work were conducted in the absence of external mass transfer limitations.

Typically, in the literature for the value of ϕ equal to 0.72, determined for the stability experiment over 15Ni-15Mg-20Al catalyst at 850 °C and atmospheric pressure, the internal mass transfer limitations would be completely neglected. However, a more rigorous analysis of mass transfer limitations including calculations of the concentration profiles inside the catalyst particles should be done to elucidate the exact impact of mass transfer. Such analysis was beyond the scope of the current work and will be performed in the future.

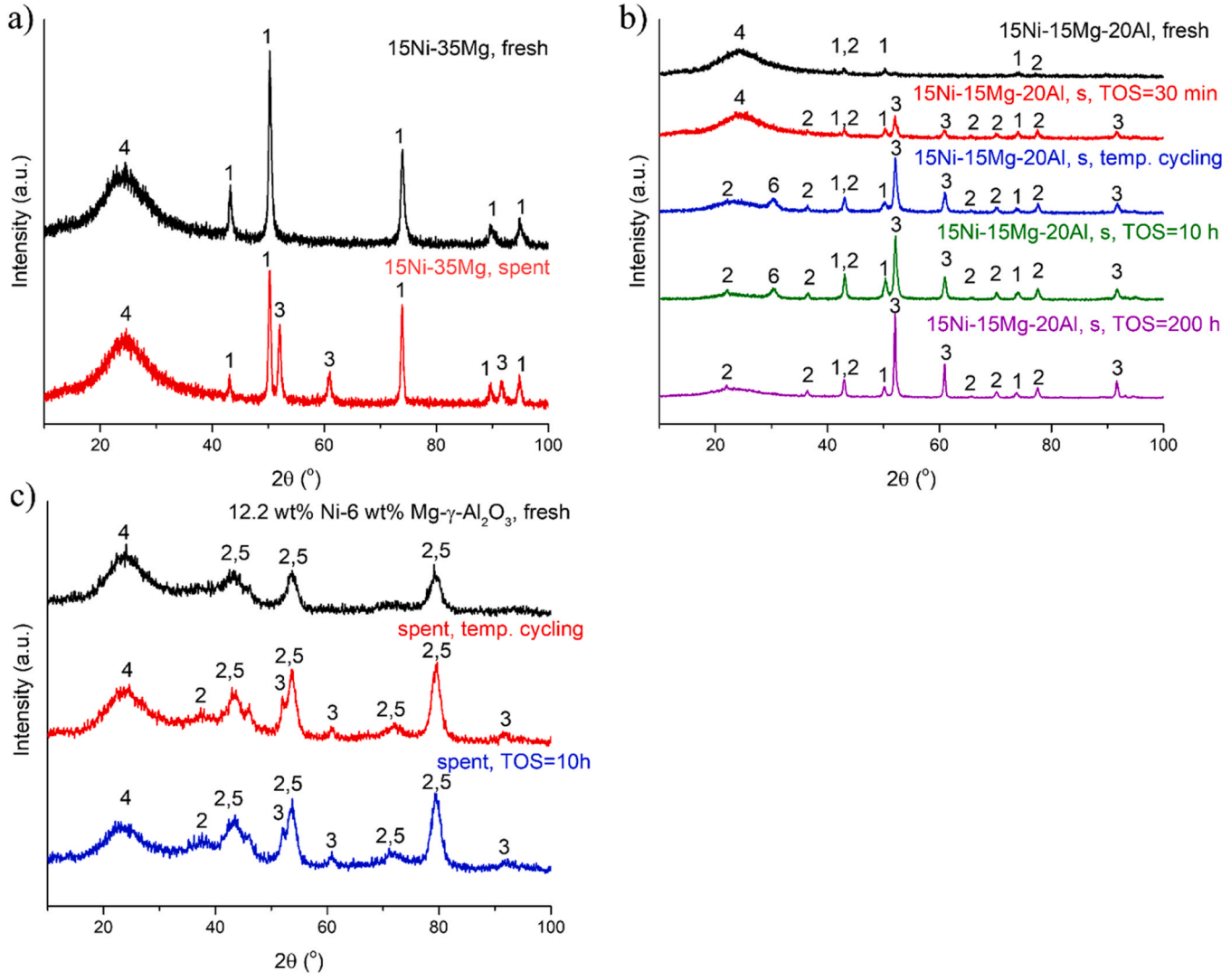

Fig. 1. XRD patterns of (a) 15Ni-35Mg, (b) 15Ni-15Mg-20Al, (c) 12 wt% Ni-6 wt% Mg/γ-Al_2O_3. Notation: 1. NiO/MgO, 2. $NiAl_2O_4$/$MgAl_2O_4$, 3. Ni^0, 4. amorphous phase, 5. γ-Al_2O_3, 6. graphite.

3. Results and discussion

3.1. Characterization of catalysts

3.1.1. XRD results

The XRD patterns of the fresh and spent catalysts are presented in Fig. 1. The patterns show that metallic Ni (Ni^0) [PDF 01–071–4655] is present in all the spent catalysts (peaks at ca. 52.5°, 61.4° and 92.4° 2θ), while the fresh catalysts do not show signs of metallic Ni, even if it was reported in the literature that Ni^{2+} species could be reduced during combustion [32,33]. NiO [PDF 01–071–4750], MgO [PDF 04–014–7440] and the respective mixtures of $Mg_{1-x}Ni_xO$ all have very similar unit cell parameters, making the precise analysis of these phases difficult. As a result, Ni^{2+} can be present in the catalyst as a separate NiO phase or by incorporation of Ni^{2+} into the MgO phase or, alternatively, $MgAl_2O_4$ [PDF 04–006–7423] phase. In the XRD pattern of the fresh 15Ni-35Mg catalyst the peak intensity ratios suggest that a $Mg_{0.7}Ni_{0.3}O$ phase [PDF 04–023–4643] has been formed. While according to TPR, NiO could strongly interacts with MgO or $MgAl_2O_4$ [34], forming even a NiO-MgO solid solution [35], the reflexes mentioned above can also be interpreted as arising from a mixture of distinct MgO and NiO phases. For the spent 15Ni-35Mg catalyst, the respective peak intensities fit better to a MgO phase which can be explained by the reduction of Ni^{2+} and formation of Ni^0, latter of which is observed as a separate set of peaks in the diffraction pattern.

According to the respective XRD pattern the crystallinity of fresh 15Ni-15Mg-20Al is very low with only a few low intensity peaks visible. These peaks can be assigned to MgO/NiO and $MgAl_2O_4$/$NiAl_2O_4$, since also $MgAl_2O_4$ and $NiAl_2O_4$ [PDF 00–001–1299] share similar cubic unit cells. These phases increase in intensity in the spent 15Ni-15Mg-20Al catalyst where also metallic nickel can be clearly observed in line with the literature [36]. Furthermore, the Ni^0 peaks become more pronounced with longer DRM tests (Fig. 1b).

As reported in [14,37] DRM catalysts exhibited $NiAl_2O_4$ phase after tests. In the current work, formation of metallic Ni can be attributed to transformations during the reaction, rather than combustion per se despite a well-known reducing role of urea [38,39].

It is worth noting that for the 15Ni-15Mg-20Al catalyst, the XRD patterns of the temperature cycling sample show a broad peak at 2θ of ca. 30° which fits very well with the main peak of carbon nanotube structure [PDF 00–058–1638]. This peak is still visible in the 10 h TOS pattern but not detected in the pattern of the material after 200 h TOS (see also TEM results below).

The prepared 12 wt% Ni-6 wt% Mg/γ-Al_2O_3 catalyst exhibits the diffraction peaks corresponding to the $MgAl_2O_4$/$NiAl_2O_4$ phase while the potential peaks of γ-Al_2O_3 (which most likely has a large amorphous content) are overlapped by the spinel phase(s). However, the small peak at 46.2° is indicative of γ-Al_2O_3 and this peak is more clearly visible in the spent catalysts. In the reduced sample examined for thermal cycles and 10 h at the constant temperature the crystallinity of the spent catalyst phases increases. As described above, peaks of cubic Ni^0 were observed also in the spent 12 wt% Ni-6 wt% Mg/γ-Al_2O_3 catalysts.

3.1.2. Analysis of catalyst morphology

Energy Dispersive X-Ray Analysis revealed the elemental composition of the SCS derived prepared and spent catalysts with the results presented in Table 2. It can be seen, that the Ni/Mg ratio in 15Ni-15Mg-20Al increased during a short test. This could be caused by an increase in the Ni particle size, which is in line with TEM results (Table 2). This ratio in 15Ni-35Mg catalyst remained the same after DRM. According to [10], catalysts with the Ni/Mg ratio above unity are highly active. In the current work Ni/Mg ratio was also above unity for both 15Ni-15Mg-20Al and 15Ni-35Mg catalysts.

The morphology of the fresh and spent Ni-Mg catalysts was studied by TEM analysis (Table 2, Fig. 2) resulting in challenges for determination of the size of metal particles, because of a poor contrast.

For the 15Ni-15Mg-20Al catalyst used in the short test, the nickel particle size was found to be 25 nm. Thermal cycles at 600—900—600 °C enlarged the metal particle size to 36 nm. As duration of the tests was prolonged, the metal particle size increased from 20 nm after 20 h TOS exposure to 30 nm after 200 h TOS, due to nickel sintering. The amounts of carbon nanotubes are large in the TEM image of the 15Ni-15Mg-20Al catalyst used in 30 min and 20 h tests. Interestingly, after a short test, the diameter of the carbon filaments was measured as 33 nm, being larger compared to the longer test, where this value was only 17 nm (Fig. 2a1, 2a3). The location of nickel particles also influences their activity [40]. In the micrographs of catalysts obtained by SCS (Fig. 2a2, 2b1), Ni particles were observed at the ends of the carbon filaments indicating a tendency to be active in catalytic reforming. Ni-Mg-Al catalyst prepared by this method displayed stable activity for a long duration run. For 15Ni-15Mg-Al catalyst examined in 200 h TOS stability test, the carbon filaments were not obviously seen (Fig. 2a4). However, nickel particles were encapsulated inside the carbon layer. Such encapsulation was also reported in [41,42]. The catalysts examined at lower temperatures exhibited the carbon nanotubes, whereas at 850 °C nickel particles were located in the carbon layer [42]. Furthermore, it was stated that larger metal particles led to higher coke deposition [43,44], which could be confirmed by TPO in the current investigation.

Regarding 12 wt% Ni-6 wt% Mg/γ-Al_2O_3 catalyst examined during thermal cycles, its average metal particle size was found as 13 nm, which is much smaller compared to the SCS derived analogue. This

Table 2
Elemental composition and the average nickel particle sizes of the catalysts. (molar ratio in the parenthesis).

Catalyst	Ni (wt%)	Mg (wt%)	Al (wt%)	O (wt%)	Ni/Mg	Ni/Al	Mg/Al	Average nickel particle size (nm)
15Ni−15Mg−20Al (f)	33.20 ± 0.29	16.25 ± 0.14	14.63 ± 0.12	35.92 ± 0.21	2.04 (0.84)	2.27 (1.0)	1.11 (1.84)	16
15Ni−15Mg−20Al (s)	46.37 ± 0.31	15.37 ± 0.13	14.54 ± 0.11	23.62 ± 0.15	3.01 (1.23)	3.19 (1.5)	1.2 (1.2)	[a]25,[b]36,[d]20,[e]30
15Ni−35Mg (f)	39.77 ± 0.32	31.29 ± 0.16	0	28.94 ± 0.19	1.3 (0.52)	n.a.	n.a.	n.d.
15Ni−35Mg (s)	41.99 ± 0.33	32.86 ± 0.16	0	25.15 ± 0.18	1.3 (0.52)	n.a.	n.a.	[a]27
12 wt% Ni−6 wt% Mg/γ-Al_2O_3 (s)	n.d.	n.d.	n.d.	n.d.	n.d.	n.d.	n.d.	[b]13,[c]9

Note:
[a] – 30 min TOS
[b] – temperature cycling
[c] – 10 h TOS
[d] – 20 h TOS
[e] – 200 h TOS.

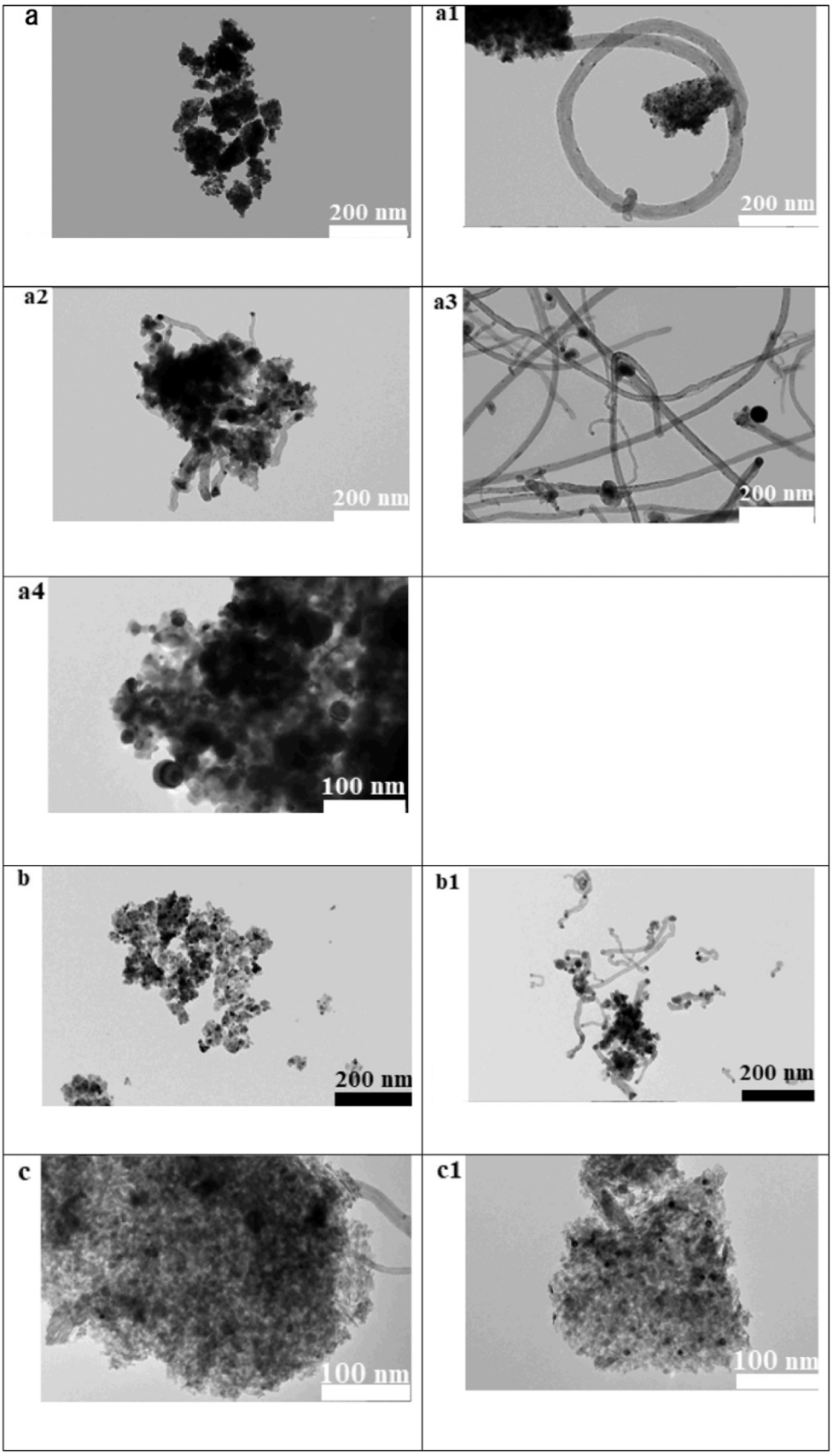

Fig. 2. TEM images (a) 15Ni-15Mg-20Al fresh, (a1) 15Ni-15Mg-20Al spent for 30 min TOS at 850 °C, (a2) 15Ni-15Mg-20Al spent in temperature cycling, (a3) 15Ni-15Mg-20Al spent for 20 h TOS at 850 °C, (a4) 15Ni-15Mg-20Al spent for 200 h TOS at 850 °C, (b) 15Ni-35Mg fresh and (b1) 15Ni-35Mg spent for 30 min TOS at 850 °C, (c) 12 wt% Ni-6 wt% Mg/γ-Al_2O_3 spent in temperature cycling, (c1) 12 wt% Ni-6 wt% Mg/γ-Al_2O_3 spent for 10 h TOS at 850 °C.

indicates higher dispersion of Ni, which is in line with XRD analysis. As time on stream increased to 10 h, the metal particles became smaller being ca. 9 nm. An analogous decrease was observed for 15Ni-15Mn-20Al reported in the previous work [45]. One potential explanation is that Ni species initially present as oxides could be reduced during DRM, thus, the particle size was decreased.

3.1.3. Textural properties

Table 3 depicts textural data of the catalysts. It was found that BET surface areas of the catalysts obtained by SCS were in the range of ca. 9—11 $m^2 \cdot g^{-1}$, similar to the literature [37,45–48]. There was almost no decrease in these values after experiments. The counterpart supported on γ-Al_2O_3 exhibited the surface area of 113 $m^2 \cdot g^{-1}$. This value is close to thew one reported in [49]. The values were almost the same after the reaction, although for the spent 15Ni-15Mg-20Al catalyst the surface area decreased by 10 %. According to the textural data, the volume of the mesopores is larger in comparison with the micropores indicating that mesoporosity is more possible. 15Ni-15Mg-20Al exhibited an increase in the total pore volume in the spent sample, which can be due to carbon accumulation on its external surface.

3.1.4. Ammonia and CO_2 TPD results

The acidic properties of 15Ni-35Mg, 15Ni-15Mg-20Al and 12 wt% Ni-6 wt% Mg/γ-Al_2O_3 catalysts was evaluated by ammonia TPD (Fig. 3, Table 4). Interestingly that 15Ni-35Al from [37] possessed lower intensity NH_3 peaks compared to the catalyst with Mg promotion and Ni-Mg catalyst without Al. The largest amount of ammonia was desorbed for 15Ni-35Mg. Some studies reported that MgO exhibited weak and medium strong acidity [50]. Moreover, it was confirmed in [51] that strong acidity was observed for Ni/MgO at ca. 660 °C. Medium acidity was not seen at 300—440 °C as the extremely low intensity peaks were observed in this temperature region. As for Ni/γ-Al_2O_3 and also 2 wt% Ni-6 wt% Mg/γ-Al_2O_3 catalysts predominance of weak Lewis acidity was defined at 139 °C [51].

Regarding basic properties, a high CO_2 desorption peak can be also seen at 510 °C in the profile of 15Ni-35Mg (Fig. 3b). The same findings were reported in [52,53], where almost similar amounts of strong basic and acidic sites were found in Ni/MgO. This catalyst also exhibited mild basicity, since desorption of CO_2 took place at 165 °C [53]. Low intensive peaks can be observed at 160 °C and 540 °C for 15Ni-15Mg-20Al catalyst (Table 4).

3.1.5. Hydrogen TPR results

TPR experiments were conducted to investigate the reduction behavior of Ni-based catalysts during DRM. It can be observed from Fig. 4 that NiO is reduced at 400–500 °C for SCS derived catalysts, pointing out to the strong interactions of this phase with the inactive component such as Al and Mg. The latter components serve as the support in SCS catalysts. Nevertheless, Ni^{2+} species were not found in the diffraction patterns.

The highest hydrogen uptake can be seen in TPR profile of 15Ni-35Mg at 542 °C, which depicts that nickel oxide was readily reduced on MgO (Table 6). Addition of Al to Ni-Mg decrease hydrogen amount for 15Ni-15Mg-20Al improving metal-support interactions. This peak was seen at ca. 280 – 600 °C. A fairly low intensity peak at 250–580 °C

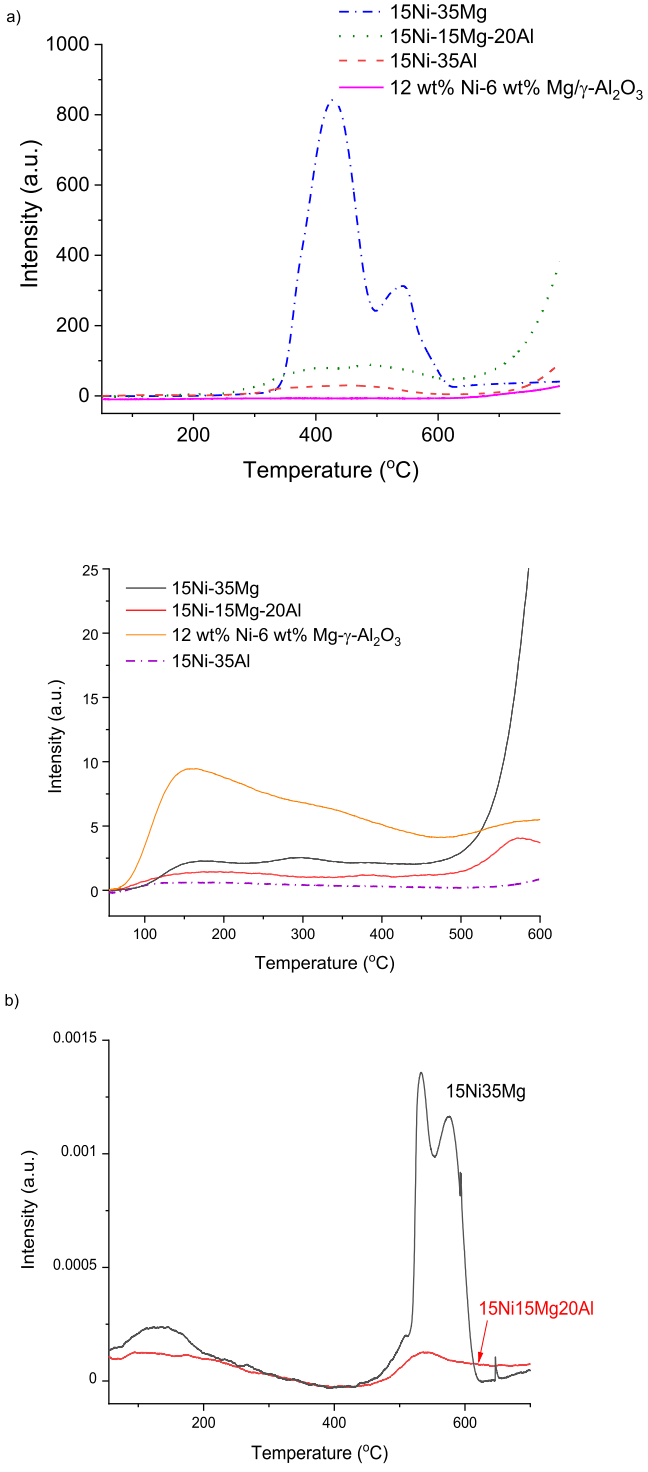

Fig. 3. (a) Ammonia and (b) CO_2 TPD profiles for Mg-containing catalysts.

Table 3
Textural data of the fresh (F) and spent (S) catalysts used in DRM for 30 min at 850 °C with GHSV of 3000 h^{-1}.

Catalyst	F/S	S_{BET} ($m^2 \cdot g^{-1}$)	V_{tot} ($cm^3 \cdot g^{-1}$)	V_{μ} ($cm^3 \cdot g^{-1}$)	V_m ($cm^3 \cdot g^{-1}$)	V_{μ}/V_m-
15Ni−15Mg−20Al	F	10	0.015	0.004	0.011	0.36
15Ni−15Mg−20Al	S	9 (90[a])	0.017	0.002	0.015	0.13
15Ni−35Mg	F	11	0.022	0.004	0.018	0.24
15Ni−35Mg	S	11 (100[a])	0.020	0.004	0.016	0.27
12 wt% Ni−6 wt% Mg/γ-Al_2O_3	F	113	0.30	0	0.30	0

[a] percentage of the retained surface area, b – 30 min TOS, c – 10 h TOS, d – 20 h TOS, e – 200 h TOS.

Table 4
Results from ammonia TPD and CO_2 TPD.

NH_3 TPD				
Catalyst	$T_{1,max}$ (°C)	$T_{2,max}$ (°C)	$T_{3,max}$ (°C)	Normalized area
15Ni−35Al	140	n.a.	n.a.	0.01
15Ni−15Mg−20Al	160	380	572	0.34
15Ni−35Mg	165	294	599	0.82
12 wt% Ni−6 wt% Mg/ γ-Al_2O_3	139	n.a.	n.a	1
CO_2 TPD				
Catalyst	$T_{1,mx}$ (°C)	$T_{2,max}$ (°C)	$T_{3,max}$ (°C)	Normalized area
15Ni−15Mg−20Al	93	36	n.a	0.47
15Ni−35Mg	129	532	577	1

Table 5
Results from hydrogen TPR.

Catalyst	$T_{1,max}$ (°C)	$T_{2,max}$ (°C)	$T_{3,max}$ (°C)	Normalized area
15Ni−35Mg	426	542	n.a.	1.0
15Ni−15Mg−20Al	306	384	484	0.52
15Ni−35Al [37]	306	384	800	0.27
12 wt% Ni−6 wt% Mg/ γ-Al_2O_3	250–580	n.a.	n.a.	0.03

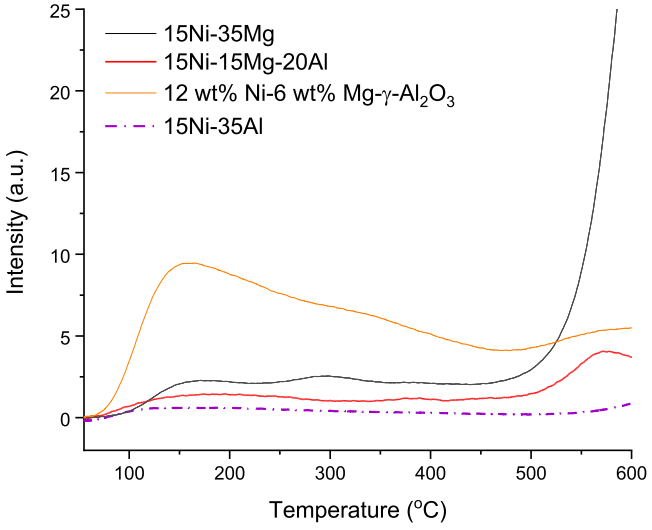

Fig. 4. Hydrogen TPR profiles of different Ni catalysts.

Table 6
Rate for carbon accumulation, calculated as normalized carbon content per g Ni and TOS (hour) in the spent catalyst determined by CHNS and calculated by CHNS analysis and H/C molar ratio. Notation: Spent catalysts were used in DRM at 850 °C for 30 min TOS unless stated otherwise.

Catalyst	Normalized C wt%·g^{-1} Ni/h	H/C molar ratio
15Ni−35Mg	0.72	0.49
15Ni−15Mg−20Al	0.19	1.53
15Ni−15Mg−20Al[a]	0.04	1.42
12Ni-Mg/γ-Al_2O_3[b]	0.25	n.a.
15Ni−35Al [37]	1	0.26

n.a. not available
[a] 200 h TOS
[b] 10 h TOS

was visible for the counterpart synthesized by impregnation. Absence of $NiAl_2O_4$ species could be explained by preferential interactions of Mg with Al_2O_3 as reported in [14] and confirmed by XRD results. Reduction of Ni^{2+} species at lower temperatures could be due to a stronger promoting behavior of Mg in the Ni-Mg-Al catalyst leading to weaker interactions with Al. Furthermore, in [54] dispersion of Ni was directly linked to the reducibility of the catalyst demonstrating that a large crystallite size causes a high hydrogen uptake at elevated temperatures. On the contrary, in the current research the small metal particle size provided a low hydrogen consumption for 12 wt% Ni-6 wt% Mg/γ-Al_2O_3.

3.1.6. Analysis of coke deposition

As a significant problem in DRM is the coke deposition, the amount of the latter was determined by CHNS analysis. The catalysts were exposed at 850 °C for a short duration and the carbon amount was normalized by the Ni weight (Table 6). It was stated in [9] that the catalyst with a larger Ni content exhibited a larger coke deposition. The lowest coke content of 1.8 wt% was observed for 15Ni-15Mg-20Al having the Ni/Mg molar ratio of 0.83 (Table 2), whereas, 15Ni-35Mg catalyst exhibited the largest carbon content. As Mg/Al ratio increases, the coke accumulation was decreased [55], referring to 15Ni-15Mg-20Al catalyst, for which this ratio was 1.8.

The H/C molar ratio varied from 0.26 to 1.53. The aromatic structure prevails at the H/C ratio approximately in the range of 0.13—1.5. 15Ni-15Mg-20Al exhibited carbon with a lower aromatic content, while 15Ni-35Al studied in [37] contained graphite coke.

15Ni-15Mg-20Al used for 20 h TOS test was also investigated by CHNS analysis. The results revealed that the coke accumulation rate after 20 h TOS (0.01 wt%·h^{-1}) was 4 times lower compared to the shorter examinations (0.04 wt%·h^{-1}), which can be interpreted by a decline of the acidic sites, where carbonaceous species can be formed.

TGA curves aiding in interpretation of the amount and type of coke are shown in Fig. 5. The tests were performed in the air and nitrogen, and temperature was elevated from room temperature to 800 °C, which was operational in DRM. When the fresh catalyst was measured in the air, the sample lost the weight slowly upon the temperature increase, whereas the weight of the coked catalyst increased at temperatures above 500 °C. Nevertheless, the weight loss in the spent Ni/MgAl catalysts was at ca. 600°C. Higher catalyst masses allowed better resistance towards coke formation bearing higher amounts of mobile oxygen vacancies [56,57]. Carbon in the 15Ni-15Mg-20Al did not contain a completely aromatic structure (see CHNS results), opposite to [58], where graphite was deposited on the Mg-Ni/Al_2O_3 catalyst possessing the Ni/Mg molar ratio of unity. TGA results of 15Ni-35Al catalyst demonstrated that the aromatic carbon was accumulated at 600 °C [37].

Oxidative behavior of the spent 15Ni-15Mg-20Al catalyst was characterized by TPO measurements (Fig. 6). The burnt carbon was defined as the amounts of CO and CO_2 formed during the tests being 12 wt% at the highest peak of 592 °C. Similar findings were reported in [59], although the peak was found symmetrical at 597 °C. As observed in the current work and [59], water was not formed. At the starting temperatures of reforming, amorphous carbon is usually deposited on the catalyst surface. In TPO examinations such type of coke is detected at 600 °C [60,61], and the aromatic carbon is identified at ca. 800 °C, while coke filaments are formed at temperatures above 600 °C [62].

3.2. Catalyst synthesis

The temperature control during solution combustion synthesis was conducted over 15Ni-15Mg-20Al catalyst (Fig. S1). Three thermocouples were used for this purpose located in the following manner: T_1 – at the highest point of the beaker, where the gas release occurred, T_2 – above the solution, T_3 – inside the solution, which turns to the gel at the initial stages. T_2 showed the highest flame temperature of ca. 1023 °C. The real synthesis temperature was far above from the pre-ignition

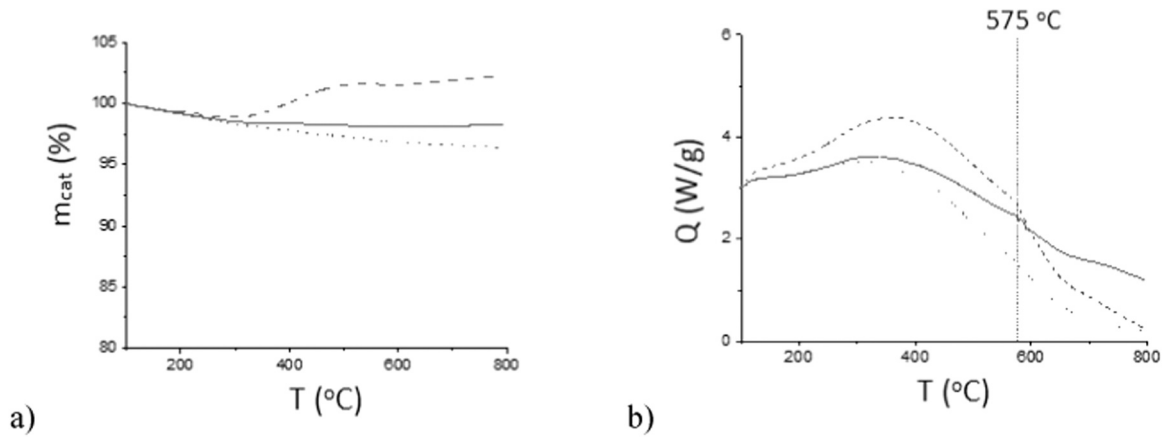

Fig. 5. a) Mass of the catalyst and b) heat release as a function of temperature during TGA for 15Ni-15Mg-20Al catalyst tested at 850 °C for 30 min TOS. Legend: fresh catalyst in N_2 flow (dot-dot line), fresh catalyst in air flow (solid line), spent catalyst in air flow (dash-dash line).

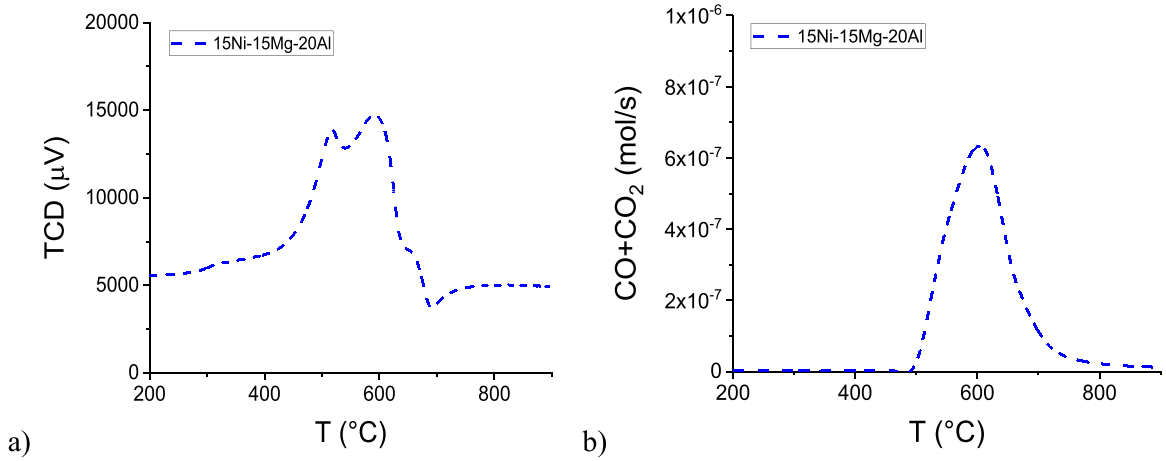

Fig. 6. (a) TPO curves and (b) amounts of the formed CO and CO_2 as a function of temperature for 15Ni-15Mg-20Al spent catalyst used in the temperature cycling test.

temperature set in the furnace (500 °C). At the combustion moment a high amount of gas was released at 695 °C. The temperature observed from T_3 was 800 °C. When using urea, NH_3 and CO were formed during combustion [63]. As reported in [27], which used glycine as a fuel, the flame temperature for Ni-Al-Cr-Mg catalyst did not reach 600 °C, and burning of glycine and metal nitrates was gradual, while in the current work the combustion was sharp over 930 s.

3.3. Catalytic results

3.3.1. Short-term catalytic tests

Dry reforming of methane was performed over 15Ni-35Mg and 15Ni-15Mg-20Al catalysts at 850 °C with duration of 30 min. In Table 7 the results of the tests are collected. To compare Ni-Mg catalysts data for 15Ni-35Al [37] were also added. According to Table 7, for these catalysts, the CO_2 transformation rate was slightly lower compared to the methane transformation rate. Subsequently, the space-time yield of CO was lower than that of hydrogen. The methane transformation rate increased for the catalysts in the following order: 15Ni-35Al < 15Ni-35Mg < 15Ni-15Mg-20Al. STY of synthesis gas increased similar to the order of the methane transformation rate. Activity of 15Ni-35Mg for the methane transformation was higher than 15Ni-35Al. While this catalyst is highly reducible in hydrogen atmosphere, it did not demonstrate high values of transformation rates and space-time yields, which can be due to its low crystallinity as seen in the XRD pattern.

Table 7 also demonstrates an optimal H_2/CO ratio equal to 1.1 for the 15Ni-15Mg-20Al catalyst with the best catalytic performance. For other catalysts, more hydrogen was obtained from CH_4 cracking, with anticipated formtion of larger carbon amounts. Based on CHNS analysis, the spent 15Ni-15Mg-20Al catalyst possesses indeed the lowest amount of carbon (Table 6).

It is difficult to find a correlation between hydrogen consumption

Table 7
Results of catalytic test for duration of 30 min, T = 850 °C, CH_4:CO_2:Ar = 1:1:1, GHSV = 3000 h^{-1}.

Catalyst	r_{CH4} ($mol \cdot s^{-1} \cdot g_{Ni}^{-1}$)	r_{CO2} ($mol \cdot s^{-1} \cdot g_{Ni}^{-1}$)	$rate_{CH4}$/ $rate_{CO2}$	TOF_{CH4} (s^{-1})	STY_{H2} ($mol \cdot s^{-1} \cdot g_{Ni}^{-1}$)	STY_{CO} ($mol \cdot s^{-1} \cdot g_{Ni}^{-1}$)	CB (%)	Deactivation rate (% $\cdot min^{-1} \cdot g_{cat}^{-1}$)[a]	H_2/ CO
15Ni−35Mg	$1.0 \cdot 10^{-4}$	$0.94 \cdot 10^{-4}$	1.1	0.16	$1.9 \cdot 10^{-4}$	$1.3 \cdot 10^{-4}$	66	0	1.5
15Ni−15Mg−20Al	$2.5 \cdot 10^{-4}$	$2.2 \cdot 10^{-4}$	1.1	0.13	$4.7 \cdot 10^{-4}$	$3.1 \cdot 10^{-4}$	69	0.13	1.1
15Ni−35Al [37]	$0.75 \cdot 10^{-4}$	$0.70 \cdot 10^{-4}$	1.1	0.006	$1.5 \cdot 10^{-4}$	$1.0 \cdot 10^{-4}$	74	0.03	1.5

[a] Deactivation rate is calculated during the decrease in CH_4 conversion per time and catalyst mass

and the methane transformation rate (Fig. S2a). 15Ni-35Al with a lower methane transformation rate has stronger metal-support interactions similar to the catalyst with Mg addition, which (15Ni-15Mg-20Al) exhibited a higher rate. The relative amount of hydrogen uptake was the highest for 15Ni-35Mg with the methane transformation rate of $1.0 \cdot 10^{-4}$ $mol \cdot s^{-1} \cdot g_{Ni}^{-1}$. Hence, the direct correlation between hydrogen consumption and methane transformation rate could not be established. A better correlation is observed in the dependence of the coke amount on the methane transformation rate as seen in Fig. S2a. Carbon is accumulated more intensively, when the methane transformation rates are slower i.e. for 15Ni-35Al and 15Ni-35Mg. Moreover, 15Ni-15Mg-20Al catalyst exhibited a low amount of coke. Since different catalyst masses were used for catalytic tests an influence of the relative amounts of acidic and basic sites on the methane transformation rate cannot be directly seen in Fig. S2b. A low Ni/Mg molar ratio (Ni/Mg =0.85) indicates a high catalytic activity of 15Ni-15Mg-20Al catalyst. Furthermore, presence of $MgAl_2O_4$ phase also influenced activity of the Mg-modified catalyst contributing to the synergy between Ni and Mg [9]. While on one side, Ni particles activate CH_4 by cracking giving hydrogen, on the other side, Mg enhances CO_2 adsorption, which can decrease the carbon formed [64].

15Ni-35Mg exhibited the lowest value of carbon balance. This means a large coke deposition, even if deactivation was not observed, according to Table 7. On the other hand, 15Ni-15Mg-20Al showed high values of the reaction rates and the product yields, although for this catalyst, deactivation was the highest, and the carbon balance was low (Fig. S3).

3.3.2. *Effect of temperature on activity and selectivity*

DRM tests were conducted over 15Ni-15Mg-20Al and 12 wt% Ni-6 wt% Mg/γ-Al_2O_3 catalysts during thermal cycles at 600—900—600 °C. The data are given in Fig. 7 and Table 8 with the final values at 600 °C. It can be seen, that transformation rates of reacting gasses and space-time yields of products increased with temperatures as expected. At the second cycle the catalysts retained stable activity, therefore metal sintering did not occur.

The reduced 12 wt% Ni-6 wt% Mg/γ-Al_2O_3 catalyst demonstrated a lower methane transformation rate at initial 600°C compared to non-reduced 15Ni-15Mg-20Al. The CO_2 transformation rate was higher for the latter catalyst than the methane transformation rate. When the methane transformation rate is lower for SCS catalyst, then the carbon release and the hydrogen yield are also lower indicating that CH_4 dissociation is not favorable at 600 °C. The reason lies in the thermodynamic limitations, therefore a high activation energy was observed for 15Ni-15Mg-20Al being 45 $kJ \cdot mol^{-1}$. At elevated temperatures and the second evaluation at 600°C, the CO_2 transformation rate was slightly lower than the methane transformation rate. At these temperatures, CO disproportionation can take place, because CO space-time yield decreased and CO_2 was formed. However, the H_2/CO ratio became 1.1. At this ratio, carbon is not usually deposited, taking into account CHNS results, according to which 15Ni-15Mg-20Al exhibited a small amount of coke.

For 12 wt% Ni-6 wt% Mg/γ-Al_2O_3 catalyst, the CH_4 transformation rate was higher than the CO_2 transformation rate, therefore the H_2/CO ratio was close to unity during the entire test. Low yields were observed for the reduced catalyst prepared by the incipient wetness impregnation.

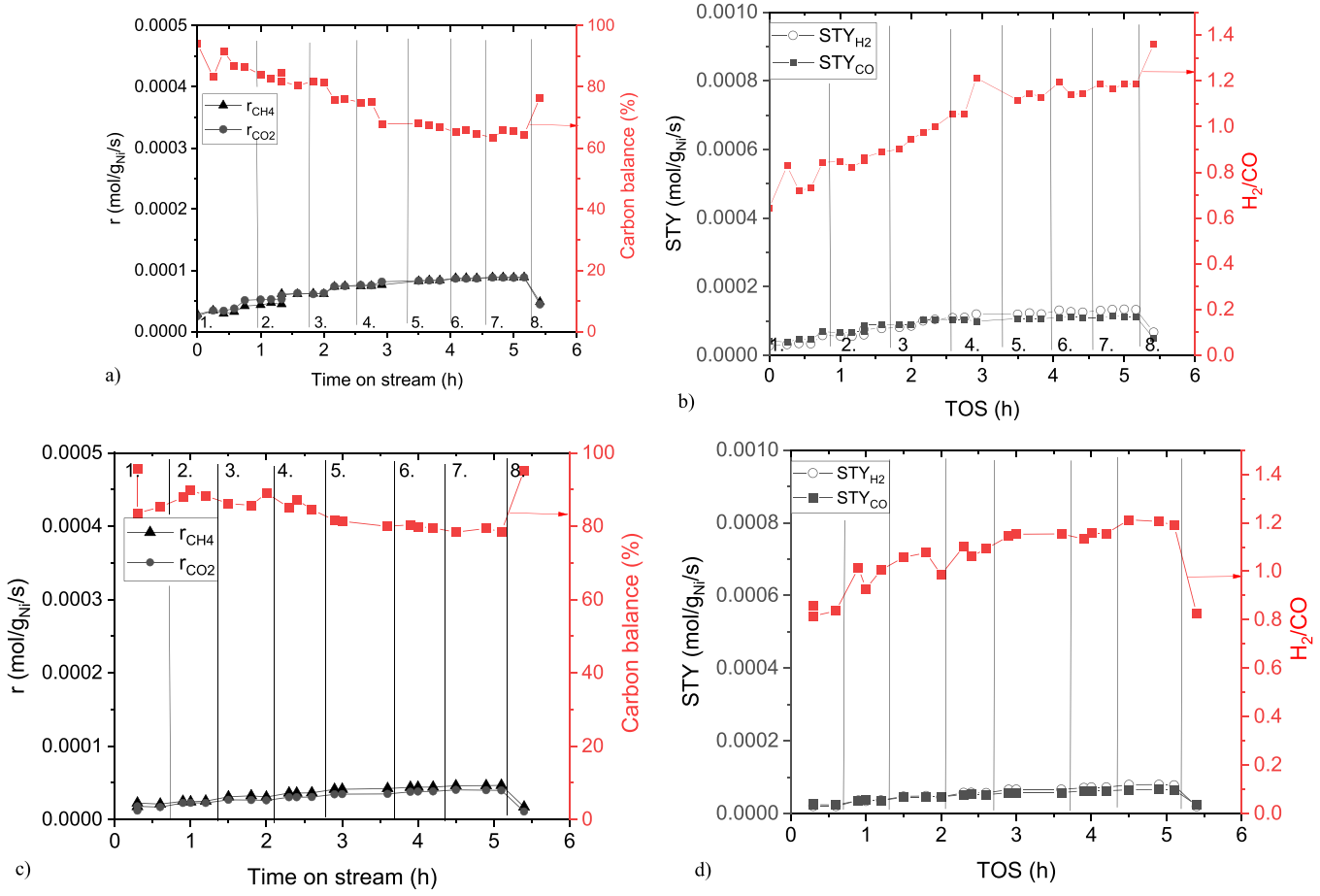

Fig. 7. Catalytic data of temperature cycling test over Ni-Mg catalysts. (a), (c) Rates for methane and CO_2 transformations and carbon balance, (b), (d) space-time yields of H_2 and CO and H_2/CO ratio in DRM over (a), (b) 15Ni-15Mg-20Al, (c), (d) 12 wt% Ni-6 wt% Mg-γ-Al_2O_3. Conditions: V_{cat} = 2 mL, GHSV = 3000 h^{-1}. Notation: 1. 600 °C, 2. 650 °C, 3. 700 °C, 4. 750 °C, 5. 800 °C, 6. 850 °C, 7. 900 °C and 8. 600 °C.

Table 8
The results of temperature cycling tests over 15Ni-15Mg-20Al and 12 wt% Ni-6 wt% Mg/γ-Al_2O_3.

Entry	Catalyst	$r_{CH4,600\,^{\circ}C}$ ($mol \cdot g_{Ni}^{-1} \cdot s^{-1}$)	$r_{CO2,\,600\,^{\circ}C}$ ($mol \cdot g_{Ni}^{-1} \cdot s^{-1}$)	$TOF_{CH4,600\,^{\circ}C}$ (s^{-1})	$CB_{600\,^{\circ}C}$ %	$r_{CH4,850\,^{\circ}C}$ ($mol \cdot g_{Ni}^{-1} \cdot s^{-1}$)	$r_{CO2,\,850\,^{\circ}C}$ ($mol \cdot g_{Ni}^{-1} \cdot s^{-1}$)	$CB_{850\,^{\circ}C}$ %	$STY_{H2,850\,^{\circ}C}$ ($mol \cdot g_{Ni}^{-1} \cdot s^{-1}$)	$STY_{CO,850\,^{\circ}C}$ ($mol \cdot g_{Ni}^{-1} \cdot s^{-1}$)	H_2/CO	E_A ($kJ \cdot mol^{-1}$)
1	15Ni−15Mg−20Al	$2.9 \cdot 10^{-5}$ ($4.8 \cdot 10^{-5}$)	$3.4 \cdot 10^{-5}$ ($4.4 \cdot 10^{-5}$)	0.006	94 (77)	$8.8 \cdot 10^{-5}$	$8.7 \cdot 10^{-5}$	67	$1.3 \cdot 10^{-4}$	$1.1 \cdot 10^{-4}$	1.1	45 (600−750) 6 (800−900)
2	12 wt% Ni−6 wt% Mg/γ-Al_2O_3	$1.8 \cdot 10^{-5}$ ($4.8 \cdot 10^{-5}$)	$1.2 \cdot 10^{-5}$ ($4.4 \cdot 10^{-5}$)	0.004	96 (95)	$4.4 \cdot 10^{-5}$	$3.8 \cdot 10^{-5}$	80	$7.1 \cdot 10^{-5}$	$6.3 \cdot 10^{-5}$	1.2	80 (600−750) 9 (800−900)

The non-reduced supported catalyst was also examined (the results are not shown). This catalyst was almost inactive even at elevated temperatures (850–900 °C). Thermodynamic limitations are also observed for this catalyst, and the activation energies at temperatures ranges of 600–750 °C and 800–900 °C are 81 and 9 $kJ \cdot mol^{-1}$, respectively, being higher than that for SCS derived catalyst.

High catalytic performance of 15Ni-15Mg-20Al catalyst during the temperature cycling test is due to a relatively small average metal particle size of this catalyst being 16 nm (Table 2). However, the metal particles sintered during a temperature cycling test giving the average metal particle size after the test of 36 nm. In comparison to the performance of 12 wt% Ni-6 wt% Mg/γ-Al_2O_3, 15Ni-15Mg-20Al was more active. A low activity of the former catalyst is partially explained by a low hydrogen uptake of this catalyst (Table 5). The fresh 12 wt% Ni-6 wt % Mg/γ-Al_2O_3 catalyst contained $MgAl_2O_4$, γ-Al_2O_3, while neither Ni nor NiO peaks were visible (Fig. 1c). During temperature cycling, however, metallic nickel, Ni^0 peak appeared in the XRD pattern.

3.3.3. Stability examination

The stability test was conducted over the SCS derived catalyst with duration of 20 h TOS. Cooling between the experiments is taken into account, and the test was continued in the following day. The test results are demonstrated in Fig. 8 and Table 9, where the values at 20 h are shown in parenthesis. The nickel supported catalyst was also studied for 10 h TOS to compare with the activity of 15Ni-15Mg-20Al (Fig. 9).

The transformation rates of reacting gasses were stable for 15Ni-15Mg-20Al (Fig. 8). It was stated in [67] that a high Ni/Mg molar ratio leads to a decrease in the catalytic performance. However, it is noteworthy that deactivation calculated for the methane transformation rate did not occur, despite high Ni/Mg molar ratios of Mg-containing catalysts used in the present research. While 12 wt% Ni-6 wt% Mg/γ-Al_2O_3 was stable during 10 h of the reaction, it exhibited lower activity compared to the SCS derived analogue (Fig. 9a, b). Differences in activity could be related to location of nickel particles within the support, while in the TEM image of 15Ni-15Mg-20Al nickel particles were located at the end of carbon nanotubes.

For 15Ni-15Mg-20Al, initially an induction period was observed. As seen in Fig. 8, conversion and yield values increased in first 6—8 h indicating its activation until it reached maximum values, although the transformation rates and the space-time yields underwent an insignificant decline, being stable for further 10 h. In [68] activation of Ni-CeO_2-ZrO_2/Al_2O_3 took place, however, conversion and yields did not decrease.

The transformation rate of CO_2 for 12 wt% Ni-6 wt% Mg/γ-Al_2O_3 was lower than the transformation rate of methane. The same trend was observed for 15Ni-15Mg-20Al catalyst. The space-time yields of H_2 were higher than the space-time yields of CO respectively, and the H_2/CO ratio was slightly higher than unity (1.1–1.2). The carbon balance over 15Ni-15Mg-20Al was close to ca. 70 %, whereas the carbon balance over the supported catalyst was slightly lower than 80 %. A higher carbon balance, according to the reaction, indicates the lower coke deposition.

For comparison, two catalysts from different studies can be compared. The methane conversion over NiO/La_2O_3 prepared by the incipient wetness impregnation was initially 20 % and sharply decreased after 1 h TOS [69]. When reaching 20 h TOS this catalyst deactivated almost completely. Compared to the impregnated counterpart, Ni-La_2O_3 catalyst synthesized via the solution combustion demonstrated an increase in the methane conversion from 20 % to 75 % by 40 h TOS being stable for 50 h [70]. However, a slight decline was observed for the last 10 h of DRM test. This comparison shows that SCS catalysts can be a promising alternative for DRM. Note that both catalysts were reduced prior DRM tests.

According to Table 9, Ni/Mg-Al-O catalyst exhibited high activity during initial 2 h with a continuous decline in methane and CO_2 conversion by 20 h TOS. H_2/CO ratio was relatively stable being 1.0 [65]. The Raman spectroscopy results showed that graphitic type of coke was

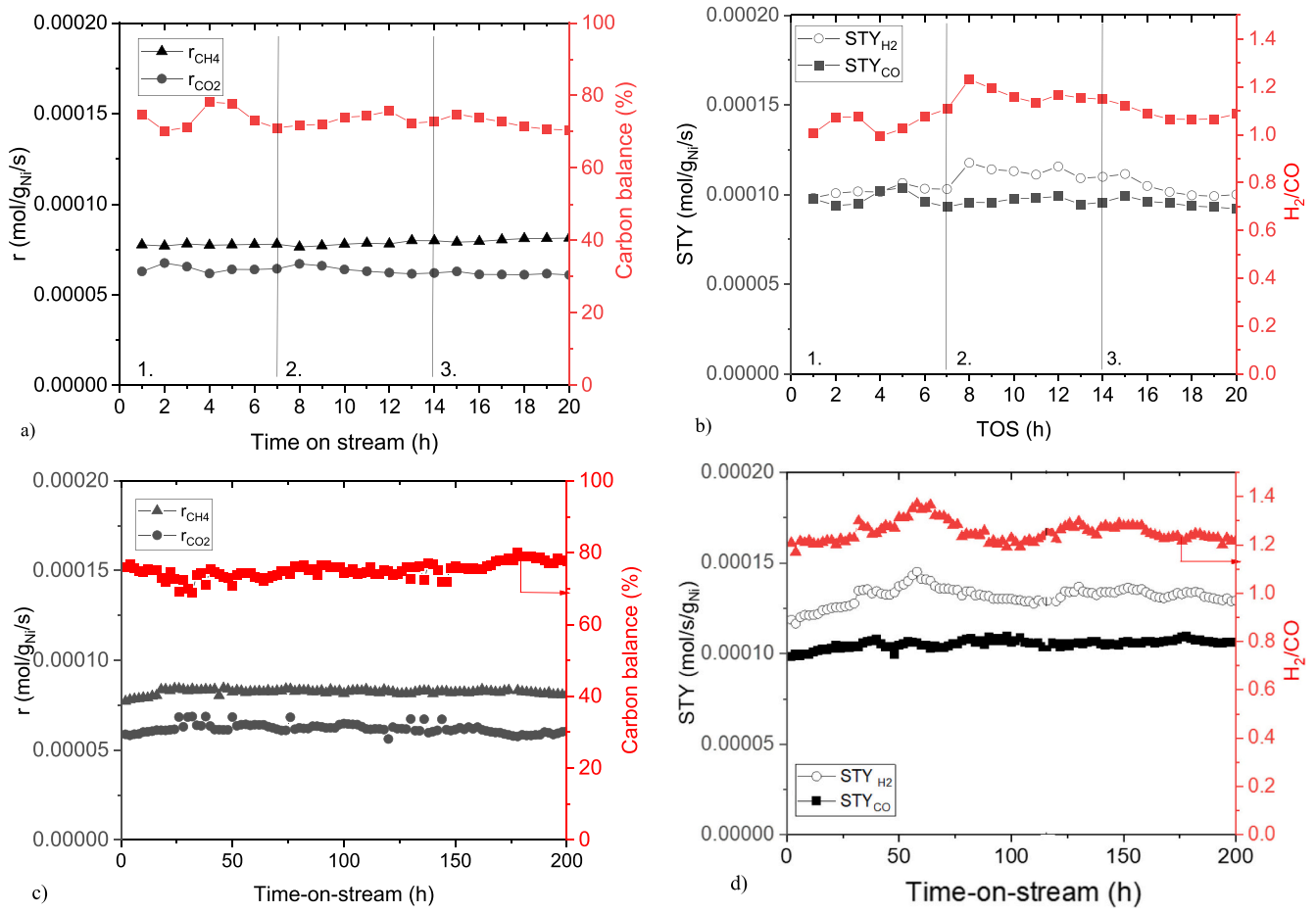

Fig. 8. (a), (c) Rate for methane and CO_2 transformation and carbon balance (a) 20 h TOS and (c) 200 h TOS), (b), (d) space time yields (STY) of H_2 and CO and H_2/CO ratio in dry methane reforming over 15Ni-15Mg-20Al for (b) 20 h and (d) 200 h TOS. Conditions: GHSV= 3000 h^{-1} at 850 °C.

Table 9
The results from stability tests for 15Ni-15Mg-20Al and 12 wt% Ni-6 wt% Mg/γ-Al_2O_3.

Catalyst	r_{CH4} (mol·s^{-1}·g_{Ni}^{-1}) Conversion, %	r_{CO2} (mol·s^{-1}·g_{Ni}^{-1})	TOF_{CH4} (s^{-1})	STY_{H2} (mol·s^{-1}·g_{Ni}^{-1})	STY_{CO} (mol·s^{-1}·g_{Ni}^{-1})	H_2/CO	CB (%)	Deactivation rate (%)
15Ni−15Mg−20Al[a]	$7.7\cdot10^{-5}$ ($8.1\cdot10^{-5}$) 97	$5.9\cdot10^{-5}$ ($6.4\cdot10^{-5}$) 96	0.08	$1.2\cdot10^{-4}$ ($8.1\cdot10^{-5}$)	$9.8\cdot10^{-5}$ ($6.1\cdot10^{-5}$)	1.2 (1.2)	76 (78)	0
15Ni−15Mg−20Al[b]	$7.8\cdot10^{-5}$ ($8.1\cdot10^{-5}$) 90	$6.3\cdot10^{-5}$ ($6.1\cdot10^{-5}$) 77	0.09	$9.8\cdot10^{-5}$ ($1.0\cdot10^{-4}$)	$9.8\cdot10^{-4}$ ($9.2\cdot10^{-5}$)	1.0 (1.1)	75 (70)	0
12 wt% Ni−6 wt% Mg/ γ-Al_2O_3[c]	$4.2\cdot10^{-5}$ ($4.4\cdot10^{-5}$) 87	$3.6\cdot10^{-5}$ ($3.9\cdot10^{-5}$) 80	n.d.	$6.7\cdot10^{-5}$ ($6.9\cdot10^{-5}$)	$5.8\cdot10^{-5}$ ($5.8\cdot10^{-5}$)	1.1 (1.2)	81 (76)	0
Ni/Mg-Al-O [65]	n.d. 82	n.d. 89	n.d.	n.d.	n.d.	1.0	n.d.	0.01
15 wt% Ni/hydrotalcite [66]	n.a. 97	n.d. 95	n.d.	n.d.	n.d.	0.9	n.d.	0.0014

n.d. not determined
[a] 200 h TOS
[b] [d]0 h TOS
[c] 10 h TOS

deposited on the catalyst surface. By TGA findings, the total weight loss was 30 %. In the present work an increase in the weight loss of 15Ni-15Mg-20Al catalyst indicates its higher coke resistance compared to Ni/Mg-Al-O sample. TPO results revealed that the spent 15 wt% Ni/hydrotalcite having a high activity exhibited low carbon accumulation rate [66]. The type of coke in the latter and 15Ni-15Mg-20Al catalysts was filamentous. It was reported that such filaments do not affect the catalytic performance, therefore, the catalysts remain stable during a long period.

Acidity/basicity plays a crucial role in selection of adequate promoters and supports. Acidic supports (Al_2O_3, SiO_2) are more likely preferential for methane dissociation giving carbon as a result. Basic supports (MgO, $MgAl_2O_4$, CeO_2, La_2O_3) favor CO_2 dissociation [71]. It was reported in [72] that CO_2 is adsorbed on the support surface forming $CO_2^{\delta-}$ species, which acted as intermediates to produce CO. The amounts of carbon deposited on the catalyst surface can be limited, since the

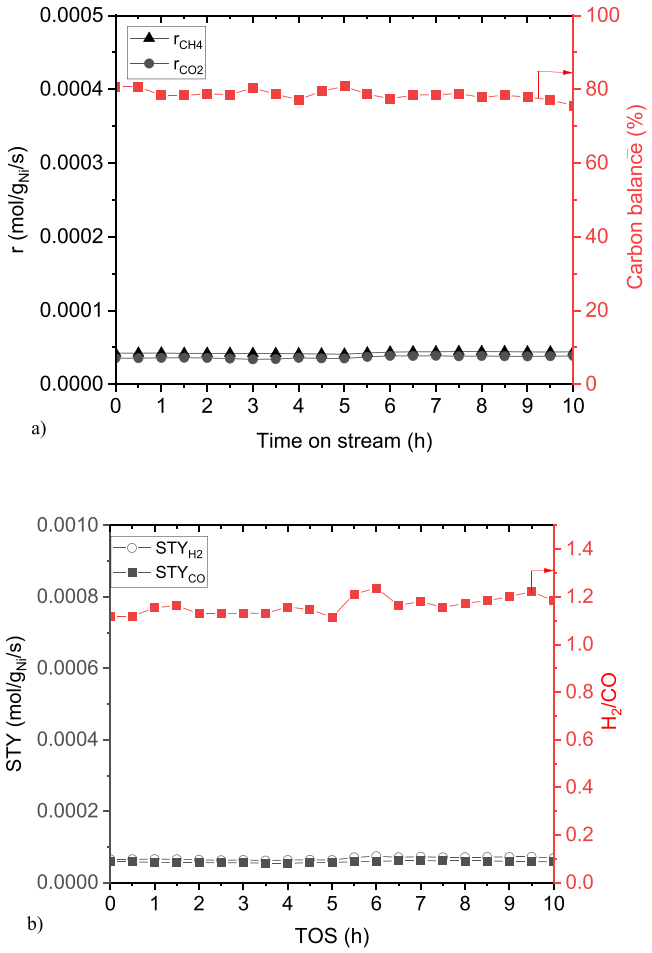

Fig. 9. (a), (c) Rate for methane and CO_2 transformation and carbon balance (a) 10 h TOS and (b), space time yields (STY) of H_2 and CO and H_2/CO ratio in dry methane reforming over 12 wt% Ni-6 wt% Mg-γ-Al_2O_3 for (b) 10 h TOS. Conditions: GHSV = 3000 h^{-1} at 850 °C.

carbon species are oxidized and react with MgO, forming $MgCO_3$. However, the 15Ni-15Mg-20Al exhibits the $MgAl_2O_4$ phase, which does not decompose because of its high stability at 1500°C [73], not providing oxygen species. It is noteworthy that $NiAl_2O_4$ is also important in coke removal. According to [74], at the alumina interface nickel aluminate was formed giving oxygen:

$$3Al_2O_3 + 2Ni^{2+} \rightarrow 2NiAl_2O_4 + 2Al^{3+} + 0.5O_2$$

At the nickel oxide interface, the spinel was obtained from nickel oxide, Al^{3+} and oxygen:

$$3NiO + 2Al^{3+} + 0.5O_2 \rightarrow NiAl_2O_4 + 2Ni^{2+}$$

Therefore, coke can be oxidized by oxygen from Ni^{2+} species. However, $NiAl_2O_4$ was not identified in the XRD pattern. For 15Ni-15Mg-20Al, the metallic nickel peak is increasing when increasing TOS. Thus, oxygen bound in Ni^{2+} can facilitate coke removal.

3.3.4. Stability test for 200 h time-on-stream

15Ni-15Mg-20Al catalyst was chosen for stability examination for 200 h considering svereal results, namely a low coke deposition, activity and stability for 20 h (Fig. 8).

As for 20 h DRM test, the induction period was also observed for 15Ni-15Mg-20Al in the longer-term experiment. At the first hour, the transformation rates of CH_4 and CO_2 were $7.72{\cdot}10^{-5}$ mol·s^{-1}·g^{-1} and $5.88{\cdot}10^{-5}$ mol·s^{-1}·g^{-1}, respectively, and increased after 24 h to $8.43{\cdot}10^{-5}$ mol·s^{-1}·g^{-1} and $6.15{\cdot}10^{-5}$ mol·s^{-1}·g^{-1}. STY_{H2} achieved the maximal value of $1.45{\cdot}10^{-4}$ mol·s^{-1}·g^{-1} after 58 h. The STY_{CO} did not undergo changes until the end of the test. The synthesis gas ratio was 1.2 indicating a higher hydrogen yield compared to CO pointing out on minimal RWGS reaction was minimal. The carbon balance changed in the range of ca. 69–80 %. According to CHNS analysis, the coke accumulation rate was decreasing, while the reaction duration became longer, changing in the following order: 4.2 wt% C·h^{-1} (30 min TOS) > 1.3 wt% C·h^{-1} (20 h TOS) > 0.01 wt% C·h^{-1} (200 h TOS). As the catalyst becomes more active in DRM due to metallic nickel, more carbon was removed probably due to magnesium aluminate spinel. In TEM image of 15Ni-15Mg-20Al used for 200 h, no carbon nanotubes were found and in addition metal sintering did not occur.

4. Conclusions

Mg-containing Ni catalysts were prepared by the solution combustion synthesis and the incipient wetness impregnation. According to the diffraction patterns, the fresh Ni-Mg catalyst is composed of nickel oxide and MgO, while for fresh 15Ni-15Mg-20Al in addition to these phases magnesium aluminate was identified. The surface area was large for γ-Al_2O_3 supported catalyst being 113 $m^2{\cdot}g^{-1}$, whereas two SCS derived catalysts possess surface area of 10–11 $m^2{\cdot}g^{-1}$ characteristic for these materials.

A high dispersion of catalysts indicated strong metal-support interactions, which enhanced catalytic activity. For 12 wt% Ni-6 wt% Mg/γ-Al_2O_3 catalyst, the metal particle size was lower, therefore metal-support interactions were stronger. Moreover, nickel particles were localized inside the support, as shown in the TEM image of the catalyst used in temperature cycling and 10 h TOS test. This led to the lower transformation rates and the synthesis gas yield. For Ni-Mg-Al obtained by SCS, the position of metal particles at the end of carbon nanotubes can be linked to their activity. Not only low acidity was observed for SCS Ni-Mg-Al catalyst, but also low intensity peaks in CO_2 TPD profiles demonstrated low basicity of this catalyst. The supported catalyst exhibited a higher amount of weak acidic sites at a low temperature. For Ni-Mg catalyst, both strong acidity and basicity at higher temperatures were observed. Compared to Ni-Mg-Al catalyst, Ni-Mg exhibited a larger carbon amount. Taking into account all observations, the former catalyst was tested for 200 h TOS in DRM. The transformation rates increased during first 24 h, being stabilized thereafter. The yield of the products was relatively stable despite small fluctuations, and the H_2/CO ratio was slightly higher than unity. Carbon accumulation for Ni-Mg-Al decreased with time on stream. Furthermore, carbon nanotubes were not seen in the TEM image. Thus, Ni-Mg-Al catalysts prepared by the solution combustion method can be effective for DRM at least at the tested conditions, namely GHSV of 3000 h^{-1} and still limited time-on-stream compared to the industrial requirements.

CRediT authorship contribution statement

Peuronen Anssi: Investigation. **Lastusaari Mika:** Investigation. **Tirri Teija:** Investigation. **Tungatarova Svetlana A.:** Writing – review & editing, Supervision, Funding acquisition, Conceptualization. **Baizhumanova Tolkyn S.:** Supervision, Investigation. **Kassymkan Kaisar:** Investigation. **Kaumenova Gulnar N.:** Investigation. **Manabayeva Alua M.:** Writing – original draft, Methodology, Investigation, Conceptualization. **Zhumabek Manapkhan:** Investigation. **Mäki-Arvela Päivi:** Writing – original draft, Supervision. **Zhumadullaev Daulet A.:** Investigation. **Vajglová Zuzana:** Investigation. **Shoganbek Dinmukhamed:** Investigation. **Martinéz-Klimov Mark:** Investigation. **Yevdokimova Olha:** Investigation. **Murzin Dmitry Yu.:** Writing – review & editing, Supervision, Conceptualization.

Declaration of Competing Interest

The authors declare that they have no known competing financial

interests or personal relationships that could have appeared to influence the work reported in this paper.

Acknowledgements

This research has been funded by the Committee of Science of the Ministry of Science and Higher Education of the Republic of Kazakhstan (Grant No. BR24992995). The authors express deep gratitude to Institute of Biomedicine, University of Turku, which receives financial support from Biocenter Finland.

Appendix A. Supporting information

Supplementary data associated with this article can be found in the online version at doi:10.1016/j.cattod.2025.115261.

Data availability

Data will be made available on request.

References

[1] Q. Song, R. Ran, X. Wu, Z. Si, D. Weng, Dry reforming of methane over Ni catalysts supported on micro- and mesoporous silica, J. CO_2 Util. 68 (2023) 102387.
[2] Z. Liu, Z. Deng, S.J. Davis, C. Giron, P. Ciais, Monitoring global carbon emissions in 2021, Nat. Rev.: Earth Env 3 (2022) 217–219.
[3] Y. Zhang, Circular economy innovations: balancing fossil fuel impact on green economic development, Heliyon 10 (2024) e36708.
[4] Z. Li, T. Yang, S. Yuan, Y. Yin, E.J. Devid, Q. Huang, D. Auerbach, A.W. Kleyn, Boudouard reaction driven by thermal plasma for efficient CO2 conversion and energy storage, J. Energy Chem. 45 (2020) 128–134.
[5] E. Rezaei, S. Dzuryk, Techno-economic comparison of reverse water gas shift reaction to steam and dry methane reforming reactions for syngas production, Chem. Eng. Res. Des. 144 (2019) 354–369.
[6] Z. Chen, S. Yan, G. Yang, Q. Hu, Y. Chen, H. Chen, Y. Yao, H. Yang, MOF-derived carbon-based catalysts with enhanced anti-coking property for the dry reforming of methane, Carbon Capture Sci. Technol. 12 (2024) 100244.
[7] K.J. Chaudhary, A.S. Al-Fatesh, A.A. Ibrahim, A.I. Osman, A.H. Fakeeha, M. Alhoshan, N. Alarifi, A.H. Al-Muhtaseb, R. Kumar, Enhanced hydrogen production through methane dry reforming: evaluating the effects of promoter-induced variations in reducibility, basicity, and crystallinity on Ni/ZSM-5 catalyst performance, Energy Conv. Manag. t: X 23 (2024) 100631.
[8] A. González, M.A. Martínez-Cruz, B. Alcántar-Vázquez, N. Portillo-Vélez, H. Pfeiffer, H.A. Lara-García, Influence of NiO into the CO_2 capture of Li_4SiO_4 and its catalytic performance on dry reforming of methane, Heliyon 10 (2024) e24645.
[9] M.J. Kim, J. Kim, Y.J. Kim, J.R. Youn, D.H. Kim, D. Shapiro, J. Guo, K. Lee, Surface control of Ni-Al_2O_3 dry reforming of methane catalyst by composition segregation, J. CO_2 Util. 81 (2024) 102721.
[10] O.W. Perez-Lopez, A. Senger, N.R. Marcilio, M.A. Lansarin, Effect of composition and thermal pretreatment on properties of Ni–Mg–Al catalysts for CO_2 reforming of methane, Appl. Catal. A: Gen. 303 (2006) 234–244.
[11] Y. Kwon, J. Eichler, C. Mullins, NiAl2O4 as a beneficial precursor for Ni/Al2O3 catalysts for the dry reforming of methane, J. CO2 Util. 63 (2022) 102112.
[12] J. Guo, H. Lou, H. Zhao, D. Chai, X. Zheng, Dry reforming of methane over nickel catalysts supported on magnesium aluminate spinels, Appl. Catal. A: Gen. 273 (2004) 75–82.
[13] X. Huang, Y. Ji, T. Wei, L. Jia, D. Yan, J. Li, High performance and stable mesoporous MgO–ZrO_2 supported Ni catalysts for dry reforming of methane, Curr. Res. Green. Sust. Chem. 4 (2021) 100183.
[14] G. Li, Y. Zhang, G. Zhang, Y. Sun, J. Liu, Effect of promoters on the catalytic performance of Ni-based catalysts for dry reforming of methane, Chem. Eng. Technol. 46 (2023) 918–926.
[15] M. Abbas, U. Sikander, M.T. Mehran, S.H. Kim, Exceptional stability of hydrotalcite derived spinel Mg(Ni)Al_2O_4 catalyst for dry reforming of methane, Catal. Today 403 (2022) 74–85.
[16] Dr.A. Chatla, F. Abu-Rub, A. Prakash, N. Elbashir, Highly stable and coke-resistant Zn-modified Ni-Mg-Al hydrotalcite derived catalyst for dry reforming of methane: synergistic effect of Ni and Zn, Fuel 308 (2022) 122042.
[17] S. Corthals, J. Van Nederkassel, J. Geboers, H. De Winne, J. Van Noyen, B. Moens, B. Sels, P. Jacobs, Influence of composition of $MgAl_2O_4$ supported $NiCeO_2ZrO_2$ catalysts on coke formation and catalyst stability for dry reforming of methane, Catal. Today 138 (2008) 28–32.
[18] A. Mazhar, A.H. Khoja, A.K. Azad, F. Mushtaq, S.R. Naqvi, S. Shakir, M. Hassan, R. Liaquat, M. Anwar, Performance analysis of TiO_2-modified Co/$MgAl_2O_4$ catalyst for dry reforming of methane in a fixed bed reactor for syngas (H_2, CO) production, Energies 14 (2021) 3347.
[19] A. Varma, A. Mukasyan, A. Rogachev, K. Manukyan, Solution combustion synthesis of nanoscale materials, Chem. Rev. 116 (2016) 14493.
[20] P. Summa, M. Gajewska, L. Li, C. Hu, B. Samojeden, M. Motak, P.Da Costa, Solution combustion synthesis as an alternative synthesis route for novel Ni-Mg-Al mixed-oxide catalyst for CO_2 methanation, J. CO_2 Util. 60 (2022) 101983.
[21] P. Summa, K. Świrk Da Costa, J. Gopakumar, B. Samojeden, M. Motak, M. Rønning, W. Van Beek, P. Da Costa, Optimization of Co-Ni-Mg-Al mixed-oxides CO2 methanation catalysts with solution combustion synthesis: on the importance of Co incorporation and basicity, Appl. Mat. Tod. 32 (2023) 101795.
[22] Y. Jiang, T. Huang, L. Dong, Z. Qin, H. Ji, Ni/bentonite catalysts prepared by solution combustion method for CO2 methanation, Chin. J. Chem. Eng. 26 (2018) 2361–2367.
[23] Md.J. Gazi, D. Khurana, J. Kaishyop, T. Suvra Khan, S. Bhandari, A. Bordoloi, Solution combustion derived nanoalloys: robust and efficient catalyst systems for partial oxidation of methane, Int. J. Hydr. Energy 51 (2024) 562–579.
[24] V. Danghyan, A. Kumar, A. Mukasyan, E.E. Wolf, An active and stable NiOMgO solid solution based catalysts prepared by paper assisted combustion synthesis for the dry reforming of methane, Appl. Cat. B: Env. 273 (2020) 119056.
[25] P. Sintuya, S. Charojrochkul, M. Chanthanumataporn, S. Wongsakulphasatch, S. Assabumrungrat, S. Ratchahat, Rapid fabrication of Ni supported MgO-ZrO2 catalysts via solution combustion synthesis for steam reforming of methane for hydrogen production, Int. J. Hydr. Energy 86 (2024) 58–71.
[26] M. Alvarez-Galvan, P. Lustemberg, F. Oropeza, B. Bachiller-Baeza, M. Ospina, M. Herranz, J. Cebollada, L. Collado, J. Campos-Martin, V. de la Peña O'Shea, J. Alonso, M.V. Ganduglia-Pirovano, Highly active and stable Ni/La-doped ceria material for catalytic CO_2 reduction by reverse water-gas shift reaction, ACS Appl. Mat. Interfaces 14 (2022) 50739–50750.
[27] M. Zhumabek, G. Kaumenova, D. Augaliev, Y. Alaidar, D. Murzin, S. Tungatarova, G. Xanthopoulou, S. Kotov, T. Baizhumanova, Selective catalytic reforming of methane into synthesis gas, Chem. Eng. Technol. 44 (2021) 2026–2033.
[28] T. Degen, M. Sadki, E. Bron, U. König, G. Nénert, Powder Diffr. 29 (ement S2) (2014) S13–S18.
[29] S. Gates-Rector, T. Blanton, Powder Diffr. 34 (2019) 352–360.
[30] M.S. Ferrandon, C. Byron, G. Celik, Y. Zhang, C. Ni, J. Sloppy, R.A. McCormick, K. Booksh, A.V. Teplyakov, M. Delferro, Grafted nickel-promoter catalysts for dry reforming of methane identified through high-throughput experimentation, Appl. Catal. A: Gen. 629 (2022) 118379–118393.
[31] D.Yu Murzin, Berlin. Chemical Reaction Technology, 2nd Ed., De Gruyter, 2022.
[32] G. Tang, D. Gong, H. Liu, L. Wang, Highly loaded mesoporous Ni–La_2O_3 catalyst prepared by colloidal solution combustion method for CO_2 methanation, Catalysts 9 (2019) 442–453.
[33] O.V. Netskina, K.A. Dmitruk, A.A. Paletsky, S.A. Mukha, A.A. Pochtar, O. A. Bulavchenko, I.P. Prosvirin, A.G. Shmakov, A.M. Ozerova, J.V. Veselovskaya, O. I. Mazina, O.V. Komova, Solvent-free synthesis of nickel nanoparticles as catalysts for CO_2 hydrogenation to methane, Catalysts 12 (2022) 1274–1294.
[34] A.H. Fakeeha, A. Kurdi, Y.A. Al-Baqmaa, A.A. Ibrahim, A.E. Abasaeed, A.S. Al-Fatesh, Performance study of methane dry reforming on Ni/ZrO_2 catalyst, Energies 15 (2022) 3841.
[35] M. Jafarbegloo, A. Tarlani, A.W. Mesbah, J. Muzart, S. Sahebdelfar, NiO–MgO solid solution prepared by sol–gel method as precursor for Ni/MgO methane dry reforming catalyst: Effect of calcination temperature on catalytic performance, Catal. Lett. 146 (2016) 238–248.
[36] S. Tripathy, D. Bhattacharya, Rapid synthesis and characterization of mesoporous nanocrystalline $MgAl_2O_4$ via flash pyrolysis route, J. Asian Ceram. Soc. 1 (2013) 328–332.
[37] A.M. Manabayeva, P. Mäki-Arvela, Z. Vajglová, M. Martinéz-Klimov, T. Tirri, T. S. Baizhumanova, V.P. Grigor'eva, M. Zhumabek, Y.A. Aubakirov, I.L. Simakova, D.Yu Murzin, S.A. Tungatarova, Dry reforming of methane over Ni-Fe-Al catalysts prepared by solution combustion synthesis, Ind. Eng. Chem. Res. 62 (2023) 11439–11455.
[38] L.J.I. Coleman, W. Epling, R.R. Hudgins, E. Croiset, Ni/Mg-Al mixed oxide catalyst for the steam reforming of ethanol, Appl. Catal. A: Gen. 363 (2009) 52–63.
[39] F. Siddique, S. Gonzalez-Cortes, A. Mirzaei, T. Xiao, M.A. Rafiq, X. Zhang, Solution combustion synthesis: the relevant metrics for producing advanced and nanostuctured photocatalysts, Nanoscale 14 (2022) 11806–11868.
[40] N. Habibi, Y. Wang, H. Arandiyan, M. Rezaei, Effect of substitution by Ni in $MgAl_2O_4$ spinel for biogas dry reforming, Int. J. Hydrog. Energy 42 (2017) 24159–24168.
[41] M. Castro Gutiérrez, P. Salinas Hernández, F. Morales Anzures, A. Gutiérrez Martínez, G. Mondragón Galicia, M.E. Fernández García, L. Escobar-Alarcón, F. Javier Tzompantzi Morales, R. Pérez-Hernández, MgO impregnation to Al_2O_3 supported Ni catalyst for SYNGAS production using greenhouse gases: Some aspects of chemical state of Ni species, Int. J. Hydr. Energy 52 (2024) 1131–1140.
[42] Y. Huang, X. Li, Q. Zhang, V.A. Vinokurov, W. Huang, Carbon deposition behaviors in dry reforming of CH_4 at elevated pressures over Ni/MoCeZr/$MgAl_2O_4$-MgO catalysts, Fuel 310 (2022) 122449.
[43] M.S. Lanre, A.E. Abasaeed, A.H. Fakeeha, A.A. Ibrahim, A.S. Al-Awadi, A.B. Jumah, F.S. Al-Mubaddel, A.S. Al-Fatesh, Lanthanum–cerium-modified nickel catalysts for dry reforming of methane, Catalysts 12 (2022) 715.
[44] H. Zhu, H. Chen, M. Zhang, C. Liang, L. Duan, Recent advances in promoting dry reforming of methane using nickel-based catalysts, Catal. Sci. Technol. 14 (2024) 1712–1729.
[45] A.M. Manabayeva, P. Mäki-Arvela, Z. Vajglová, M. Martinéz-Klimov, O. Yevdokimova, A. Peuronen, M. Lastusaari, T. Tirri, T.S. Baizhumanova, K. Kassymkan, G.N. Kaumenova, A.R. Brodskiy, R.O. Sarsenova, K.A. Shorayeva, D. Y. Murzin, S.A. Tungatarova, Dry reforming of methane over Mn-modified Ni-based catalysts, Catal. Lett. 154 (2024) 4780.

[46] A.M. Manabayeva, P. Mäki-Arvela, Z. Vajglová, M. Martinéz-Klimov, O. Yevdokimova, A. Peuronen, M. Lastusaari, T. Tirri, K. Kassymkan, T. S. Baizhumanova, M. Zhumabek, R.N. Sarsenova, Z.T. Zheksenbaeva, D.Yu Murzin, S.A. Tungatarova, Dry reforming of methane over rare-earth metal oxide Ni-M-Al (M = Ce, La) catalysts, Ind. Eng. Chem. Res. 62 (2023) 20588–20607.
[47] C. Alvarez-Galvan, H. Falcon, V. Cascos, L. Troncoso, S. Perez-Ferreras, M. Capel-Sanchez, J.M. Campos-Martin, J.A. Alonso, J.L.G. Fierro, Cermets Ni/($Ce_{0.9}Ln_{0.1}O_{1.95}$) (Ln = Gd, La, Nd and Sm) prepared by solution combustion method as catalysts for hydrogen production by partial oxidation of methane, Int. J. Hydrog. Energy 43 (2018) 16834.
[48] B. Abu-Zied, A.M. Asiri, Urea-based combustion process for the synthesis of nanocrystalline Ni-La-Fe-O catalysts, J. Nanomat. (2012) 428643.
[49] N.M. Kamal, W.A. Bakar, S. Toemen, R. Ali, Biodiesel production via transesterification of low rade cooking oil over heterostructure nano particles of Ni/Mg/Al_2O_3 Catalyst, IJE Trans. B: Appl. 31 (2018) 1318–1325.
[50] S. Cimino, L. Lisi, L.S. Romanucci, Catalysts for conversion of ethanol to butanol: Effect of acid-base and redox properties, Catal. Today 304 (2018) 58–63.
[51] V. Mohan, V. Venkateshwarlu, C.V. Pramod, B.D. Raju, K.S.R. Rao, Vapour phase hydrocyclisation of levulinic acid to γ-valerolactone over supported Ni catalysts, Catal. Sci. Tech. 4 (2014) 1253–1259.
[52] Q. Zhu, C. Shen, J. Wang, T. Tan, Upgrade of solvent-free acetone butanol ethanol mixture to high-value biofuels over Ni-containing MgO SiO_2 catalysts with greatly improved water-resistance, ACS Sust. Chem. 5 (2017) 8181–8191.
[53] W. Gac, Acid–base properties of Ni–MgO–Al_2O_3 materials, Appl. Surf. Sci. 257 (2011) 2875–2880.
[54] J.L. Martín-Espejo, L.P. Merkouri, J.A. Odriozola, T. Ramirez Reina, L. Pastor-Pérez, Effect of calcination temperature on the synthesis of Ni-based cerium zirconate for dry reforming of methane, Ceram. Int 50 (2024) 38406–38414.
[55] Y. Zhu, S. Zhang, B. Chen, Z. Zhang, C. Shi, Effect of Mg/Al ratio of NiMgAl mixed oxide catalyst derived from hydrotalcite for carbon dioxide reforming of methane, Catal. Today 264 (2015) 163–170.
[56] X. Sun, Y. Wang, B. Yan, Enhancing coke resistance of $Mg_{1-x}Ni_xAl_2O_4$ catalysts for dry reforming of methane via a doping-segregation strategy, ChemCatChem 15 (2023) e202300220.
[57] E. Smal, Y. Bespalko, M. Arapova, V. Fedorova, K. Valeev, N. Eremeev, E. Sadovskaya, T. Krieger, T. Glazneva, V. Sadykov, M. Simonov, Carbon formation during methane dry reforming over Ni-containing ceria-zirconia catalysts, Nanomaterials 12 (2022) 3676.
[58] B. Jin, S. Li, X. Liang, Enhanced activity and stability of MgO-promoted Ni/Al_2O_3 catalyst for dry reforming of methane: Role of MgO, Fuel 284 (2021) 119082–119090.
[59] I. Silverwood, N.G. Hamilton, C. Laycock, J. Staniforth, M. Ormerod, C. Frost, S. Parker, D. Lennon, Quantification of surface species present on a nickel/alumina methane reforming catalyst, Phys. Chem. Chem. Phys. 12 (2010) 3102–3107.
[60] K. Nagaoka, K. Seshan, K.I. Aika, J.A. Lercher, Carbon deposition during carbon dioxide reforming of methane – comparison between Pt/Al_2O_3 and Pt/ZrO_2, J. Catal. 197 (2001) 34–42.
[61] P. Wang, E. Tanabe, K. Ito, J. Jia, H. Morioka, T. Shishido, K. Takehira, Filamentous carbon prepared by the catalytic pyrolysis of CH_4 on Ni/SiO_2, Appl. Catal. A: Gen. 231 (2002) 35–44.
[62] X. Zhu, Yp Zhang, Cj Liu, CO Adsorbed infrared spectroscopy study of Ni/Al_2O_3 catalyst for CO_2 Reforming of methane, Catal. Lett. 118 (2007) 306–312.
[63] A. Khort, K. Podbolotov, R. Serrano-García, Y. Gun'ko, One-step solution combustion synthesis of cobalt nanopowder in air atmosphere: the fuel effect, Inorg. Chem. 57 (2018) 1464–1473.
[64] X. Gao, Z. Ge, G. Zhu, Z. Wang, J. Ashok, S. Kawi, Anti-coking and anti-sintering Ni/Al_2O_3 catalysts in the dry reforming of methane: Recent progress and prospects, Catalysts 11 (2021) 1003–1021.
[65] X. Fang, J. Zhang, J. Liu, C. Wang, Q. Huang, X. Xu, H. Peng, W. Liu, X. Wang, W. Zhou, Methane dry reforming over Ni/Mg-Al-O: On the significant promotional effects of rare earth Ce and Nd metal oxides, J. CO2 Util. 25 (2018) 242–253.
[66] A.R. González, Y.J.O. Asencios, E.M. Assaf, J.M. Assaf, Dry reforming of methane on Ni–Mg–Al nano-spheroid oxide catalysts prepared by the sol–gel method from hydrotalcite-like precursors, Appl. Surf. Sci. 280 (2013) 876–887.
[67] D.Y. Kalai, K. Stangeland, Y. Jin, Z. Yu, Active and stable hydrotalcite derived Ni catalysts for CO_2 reforming of methane: Comparison with catalysts by incipient wetness, J. CO_2 Util. 25 (2018) 346–355.
[68] J. Lucas, N.S. Padmanabha Naveen, M.J. Janik, K. Alexopoulos, G. Noh, D. Aireddy, K. Ding, J.A. Dorman, K.M. Dooley, Improved selectivity and stability in methane dry reforming by atomic layer deposition on Ni-CeO_2-ZrO_2/Al_2O_3 Catalysts, ACS Catal. 14 (2024) 9115–9133.
[69] R. Gomes, D. Costa, R. Junior, M. Santos, C. Rodella, R. Fréty, A. Beretta, S. Brandão, Dry reforming of methane over NiLa-Based Catalysts: Influence of synthesis method and Ba addition on catalytic properties and stability, Catalysts 9 (2019) 313.
[70] Y. Ahmad, A. Mohamed, A. Kumar, S. Al-Qaradawi, Solution combustion synthesis of Ni/La_2O_3 for dry reforming of methane: tuning the basicity via alkali and alkaline earth metal oxide promoters, RSC Adv. 11 (2021) 33734–33743.
[71] A.G.S. Hussien, K. Polychronopoulou, A Review on the different aspects and challenges of the dry reforming of methane (DRM) reaction, Nanomaterials 12 (2022) 3400.
[72] Y. Schuurman, C. Mirodatos, P. Ferreira-Aparicio, I. Rodriguez-Ramos, A. Ruiz, Bifunctional pathways in the carbon dioxide reforming of methane over MgO-promoted Ru/C catalysts, Catal. Lett. 66 (2000) 33–37.
[73] S. Hashimoto, A. Yamaguchi, Synthesis of $MgAl_2O_4$ whiskers by an oxidation-reduction reaction, J. Am. Ceram. Soc. 79 (1996) 491–494.
[74] K.H. Song, S.K. Jeong, B.H. Jeong, K.-Y. Lee, H.J. Kim, Effect of the Ni/Al ratio on the performance of $NiAl_2O_4$ spinel-based catalysts for supercritical methylcyclohexane catalytic cracking, Catalysts 11 (2021) 323.